UCID--21438

DE88 012452

Structural Evaluation of the Shippingport Reactor Pressure Vessel and Neutron Shield Tank Package for Impact and Puncture Loads

Manuscript Completed: May 1988
Date Published: June 1988

Prepared By: L. E. Fischer, C. K. Chou, T. Lu, and M. W. Schwartz

Nuclear Systems Safety Program
Lawrence Livermore National Laboratory
7000 East Avenue
Livermore, California 94550

Prepared for
Shippingport Station Decommissioning Project
Richland Operations Office
Department of Energy

Abstract

A structural evaluation of Shippingport Reactor Pressure Vessel and Neutron Shield Tank package for impact and puncture loads under the normal and hypothetical accident conditions of 10 CFR 71 was performed.

Component performance criteria for the Shippingport package and the corresponding structural acceptance criteria for these components were developed based on a review of the package geometry, the planned transport environment, and the external radiation standards and dispersal limits of 10 CFR 71.

The evaluation was performed using structural analysis methods. A demonstration combining simplified model tests and nonlinear finite element analyses was made to substantiate the structural analysis methods used to evaluate the Shippingport package. The package was analyzed and the results indicate that the package meets the external radiation standards and release limits of 10 CFR 71.

Table of Contents

List of Tables

List of Figures

ACKNOWLEDGMENTS

The authors wish to acknowledge the technical contributions made to this report by S. Bumpus, J. Hovingh, M. A. Gerhard, S. N. Shukla, D. J. Trummer, and M. C. Witte of Lawrence Livermore National Laboratory. The authors wish to thank J. J. Schreiber, manager of the Shippingport Station Decommissioning Project, and G. E. VanSickle of the Westinghouse Hanford Company for their support and comments during the structural evaluation phase and the preparation of this report. Also, many thanks to M. A. Calhoun for report preparation.

1.0 Introduction

1.1 Background

The Shippingport Atomic Power Station in Shippingport, Pennsylvania is being decommissioned and dismantled under the Department of Energy (DOE) to return the government leased property in a radiologically safe condition to its owner, the Duquesne Light Company. All radioactive material is being removed from the Shippingport Station and transported to the DOE Hanford Reservation in Richland, Washington for burial. The DOE Richland Operations Office (RL) is in charge of the Shippingport Station Decommissioning Project (SSDP).

Prior to the start of decommissioning, all of the nuclear fuel was removed from the reactor pressure vessel (RPV) and shipped offsite. Since then, the integral reactor pressure vessel/neutron shield tank (RPV/NST) was filled with a lightweight concrete material to form a transport package. The concrete-filled RPV/NST package will be transported by barge to the Hanford reservation.

Since the RPV contains radioactive components and materials, the RPV/NST package must be certified for transport, in accordance with DOE Order 5480.3, prior to shipment. DOE Order 1540.2 specifies administrative procedures to use when applying for the certification and use of a packaging. To obtain a Certification of Compliance for packaging, DOE 1540.2, Chapter II.2 requires that a Safety Analysis Report for Packaging (SARP) be prepared to demonstrate that the packaging design, manufacture, operations, and quality assurance meet DOE safety criteria. The SARP must then be submitted to the Certifying Official, Office of Security Evaluations (OSE), for review and approval.

SSDP funded the Westinghouse Hanford Company (WHC) to prepare a SARP for the RPV/NST package. The RPV/NST package was prepared by General Electric, which is the Decommissioning Operations Contractor (DOC) at Shippingport. An important aspect of the SARP is the structural evaluation of the RPV/NST package under impact and puncture conditions. SSDP funded the Lawrence Livermore National Laboratory (LLNL) to evaluate analytically the RPV/NST

package for the impact and puncture conditions. The nonlinear finite-element analysis computer codes, DYNA2D and DYNA3D (or DYNA2D/3D, or simply DYNA codes) (Refs. 1 and 2), developed by LLNL, were used in the analyses. These codes can handle many types of materials including concrete. This report documents the structural evaluation of the RPV/NST for impact and puncture conditions for input to the SARP.

1.2 Package Classification and Certification

1.2.1 Package Classification

The Shippingport RPV/NST package has an aggregate radioactivity of 16000 ±3000 Ci (Ref. 4). Under the guidelines of Packaging Review Guide (Ref. 3), this package can be classified as a Type B Category II package. It satisfies the following radioactivity limits:

$3000\ Ci < 16000\ Ci < 30000\ Ci$

$30A_2 < 1130\ A_2 < 3000A_2$

where A_2 is the maximum activity of radioactive material, other than special form radioactive material, permitted in Type A package.

1.2.2 Package Certification

For the Shippingport package, the public transport starts when the package leaves the pier of the Shippingport Station on a barge, and ends when the package enters Hanford Reservation on a transporter for final burial. This package will be used for one time shipment only.

1.3 Technical Basis for the Design of the Package

From the standpoint of safe transport of radioactive material, the external radiation standards of the 10 CFR 71 (Section 71.47) are the fundamental requirement for all packages. For Type B packages, regulations also require (Section 71.51):

1. When the packaging is subjected to tests under Section 71.71 (Normal Conditions of Transport), there would be no loss or dispersal of

radioactive contents, as demonstrated to a sensitivity of 10^{-6} A_2 per hour, no significant increase in external radiation levels, and no substantial reduction in the effectiveness of the packaging; and

2. When the packaging is subjected to tests under Section 71.73 (Hypothetical Accident Conditions), there would be no escape of other radioactive material exceeding a total amount A_2 in one week and no external radiation dose exceeding 1 rem per hour at 1 m from the external surface of the package.

The Shippingport RPV/NST package, a Type B Category II package, weighs approximately 900 tons and has the dimensions of 17.5 ft. in diameter and 40.7 ft. in length. With this weight and size, it is extremely unlikely that the loadings associated with the hypothetical accident conditions, such as a 30-foot free drop onto an unyielding surface, will occur during its one-time shipment from Shippingport Station to Hanford Reservation. Despite the low occurrence probability of these loads, the package will be evaluated for those tests specified in 10 CFR 71 to expedite the certification process.

A special characteristic of this package is that it contains only irradiated nuclear components that will not break up into small pieces even under severe crush conditions. Also, all radioactive components are cast in concrete to form a monolithic solid piece.

It was found in a study by WHC (Section 5.5.2 of Ref. 4) that the external radiation and dispersal standards of 10 CFR 71.47 and 71.51 can be met when the outer shell holds the concrete together (or the outer shell does not open up to expose the RPV directly to the outside environment) under the tests specified in Sections 71.71 and 71.73.

Based on this study, the radiation and dispersal requirements of 10 CFR 71, and the unique characteristics of this package, the following structural performance criteria were developed for the tests specified in Sections 71.71 and 71.73:

1. A containment system for leak-tightness is not needed. Instead, an integrated confinement system, the outer shell, can serve the

containment purpose for this nondispersible Type B Category II package.

Under the tests specified in 71.71 and 71.73, confinement is achieved if there is no catastrophic breakup of the system. That is, local stresses exceeding yield are acceptable for normal conditions and local rupture and puncture are acceptable for hypothetical accident conditions provided the radiation and dispersion limits are not exceeded.

2. The RPV provides radiation shielding and serves as a backup confinement system for additional protection. However, it will not be relied upon as a confinement system in the application for a transport certificate.

The structural acceptance criteria in Regulatory Guides 7.6 and 7.8 were developed for the containment system of a Type B Category I packaging containing dispersible fissile materials, such as spent fuel. These criteria are not applicable to the Shippingport RPV/NST package because it is a nondispersible, Category II package with relatively low specific activities and does not require a containment system to assure leak-tight protection.

In the absence of applicable structural acceptance criteria for Category II nondispersible packaging with relatively low specific activities, a set of criteria were developed specifically for the RPV/NST package which are deemed to be appropriate and to have sufficient margins of safety included in them to satisfy the external radiation standards set forth in 10 CFR 71. The large deformations expected in the outer shell (NST and skirt) dictates the use of strain limit criteria for structural acceptance. The limit state chosen is one that will satisfy the technical basis for design. The limit chosen is the onset of necking instability of the outer shell which is the confinement boundary material. This limit is adopted because, for a ductile material, it is the threshold beyond which rupture is possible and below which rupture is not possible. Further details are presented in Chapter 4. Other structural acceptance criteria for the RPV closure bolts and for evaluating puncture were also developed specifically for the RPV/NST package. The various criteria and

various criteria and their basis are discussed in Chapters 4 and 5 where the specific structural evaluations for impact and puncture are presented.

1.4 Objective and Approach

The objective of this work is to perform a structural evaluation of the Shippingport RPV/NST package for impact and puncture loads in accordance with 10 CFR 71.

Due to the large size of the package, it is not practical to perform full-size tests. Instead, the evaluation is based on structural analysis supplemented with benchmark tests to increase our confidence in the DYNA computer analysis codes for this specific application.

Scale-model tests were considered but were not adopted in the case of the Shippingport RPV/NST package. The main reason is that the behavior of a confined concrete (in the case of Shippingport, confined inside the RPV and between the outer shell and the RPV) is not well understood in scale-model tests, and no defendable scaling mechanism exists by which one may determine the response of the full-size RPV/NST package from the response of a scale model for the test requirements specified in 10 CFR 71.

The best practical approach to evaluating the RPV/NST package is to perform nonlinear finite-element structural analysis using computer codes that can simulate concrete behavior under a confined environment.

The concrete in the Shippingport RPV/NST package serves multiple functions and is an important part of the package. These functions are:

1. An impact-energy absorbing material through confined compression for both the normal conditions of transport and the hypothetical accident conditions.
2. A filling material to hold various parts of the package together in their respective positions.
3. A strengthening material to prevent catastrophic failure of the outer shell.

4. Additional shielding.

The DYNA codes were selected to perform the structural calculations. These codes have been used extensively in the past ten years. However, to provide additional confidence in these codes using the concrete model, especially for the special geometric characteristics of the Shippingport RPV/NST package and the confined environment of the concrete under free-drop conditions, a demonstration combining tests and finite-element analyses was performed. This demonstration includes three elements:

1. Drop tests of a model that has similar geometric characteristics of the Shippingport RPV/NST package, including the actual mechanical properties of the concrete used in the RPV/NST package.
2. Finite-element analysis of this model using DYNA codes with the concrete model.
3. Evaluation of the analytical results against the test results.

The demonstration was performed using a simplified model test and related benchmark analyses. This demonstration provides the confidence that is needed to use DYNA codes for the Shippingport RPV/NST package without full-scale testing. Section 3.0 documents the test, the associated finite-element analyses, and the comparisons.

Once confidence in the confined-concrete model in the DYNA codes is gained for the special geometry of the RPV/NST package, the structural evaluation is carried out. The structural evaluation includes impact and puncture analyses for the RPV/NST package. End drops, side drops and oblique drops were considered for the hypothetical accident conditions. The structural evaluations for impact conditions are presented in Section 4.0. Section 5 describes the evaluation of the package for puncture by a 6-inch-diameter puncture bar.

2.0 Description of RPV/NST Package

2.1 RPV/NST Package Description

The major components of the RPV/NST package, as shown in Figure 2.1, are the RPV and closure head, the thermal shield, the upper and lower core barrels, the filler plates, the bottom plate, the NST, the lifting beam and skirt, the concrete fill material, and some structural components of the reactor core, which are stored in the RPV cavity for disposal with the package.

Details of the RPV/NST package and a summary of material specifications were provided to LLNL. The following description summarizes the package from the outer surface inward to the interior of the RPV. Further detail may be found in Ref. 4.

The outer surface of the RPV/NST package is formed by the outer wall of the NST and the skirt. The NST is fabricated from 1-in.-thick steel plate, ASME Specification SA-212 Grade B. The lower portion of the tank shell includes sleeves, which allowed the four 15-in.-ID reactor-coolant inlet lines to pass through the tank to the RPV. These coolant lines were cut back at least 3 in. from the inner surface of the NST. The openings in the NST wall are covered with 1-in.-thick steel plates that are welded to the outer NST wall.

The skirt is fabricated from 1-in.-thick steel plate, ASTM Specification A-36, and is welded circumferentially to the NST outer wall. The skirt blocks the four 15-in.-ID outlet-nozzle openings to the RPV. The combination of the NST outer wall and the skirt will provide the confinement system for the package. The nominal size and weight of the entire package are 17.5 ft in diameter by 40.7 ft long and 900 tons, respectively. The support skirt includes the main lifting beam, which is connected to the RPV by means of 16 lifting studs (ASTM A-36) and is utilized for the vertical lift out of the Shippingport Power Station cavity. The lifting lugs will be removed after the lift is completed. It is important to note that the lifting operation is not part of the transportation process.

The NST annulus is filled with 120 to 130 lb/ft^3 density concrete having a minimum 28-day compressive strength of 2000 psi. The concrete mix was designed to be fluid enough to fill all holes and voids in the package during pouring operations. The 5-in. annular space between the inner wall of the NST and the RPV is filled with a 4-in.-thick blanket of fiberglass insulation and a 1-in. thickness of the same concrete material. In addition, the underside of the lifting beam is filled with this same concrete material. Concrete pour is performed in accordance with Technical Specification 99M of the site Decommissioning Operations Contractor (DOC) procedures (Ref. 5). Further information on the concrete fill material is presented in Section 2.2.3.

The RPV is cylindrical, with an inside height of 300 in., an inside diameter of 109 in., and a nominal wall thickness of 8-3/8 in. The vessel has a bottom hemispherical head. There are four inlet nozzles in the bottom head and four outlet nozzles near the middle of the vessel. The vessel cavity is also filled with concrete. The concrete fill is in accordance with Technical Specification 99Z (Ref. 5).

The RPV is formed primarily of manganese-molybdenum-carbon steel plates (ASTM-SA-302, Grade B) and a flange forging (ASTM-SA-182). The vessel shell, bottom hemispherical head, and the thicker nozzle sections were made from plates to which the stainless steel cladding was roll-bonded. The cladding in the flange sections and the thinner section of the inlet nozzle was deposited by machine welding.

The vessel was supported vertically on 24 equally spaced pads welded to the outside of the vessel below the outlet nozzles. These pads rested on horizontal, radial, cylindrical pins mounted on the heavy ring girder portion of the NST. The pins allowed the RPV to expand and contract with respect to its supporting structure without inducing high stresses. The effects of these support pads are not needed for package shipment because the void spaces are filled with concrete, which provides lateral support.

The external surface of the RPV adjacent to the NST is covered with a 4-1/2 in. thick layer of fiberglass thermal insulation, compressed to 4 in. The insulation includes wire mesh on the surface against the RPV wall, and

expanded metal and 18-gauge sheet steel on the external surface. The insulation extends upward from the bottom of the RPV to just below the RPV head.

The reactor closure head was fabricated from a forging of ASTM-508-67, Class 4, low-alloy steel. Within a 113 in. diameter, the forging is flat with a thickness of 51 in. The integral bolting flange is 23 in. thick by 154 in. OD and has 42 penetrations to accommodate the closure and lifting studs. Within the 113 in. diameter on the head, there are 18 penetrations that accommodated 12 control drive mechanisms (CDM) and 6 bypass inlet flow (BIF) supply tubes. The housings are made of Ni-Cr-Fe alloy 600 and are attached to the closure head with full penetration welds. Each nozzle penetration was severed close to the top of the head and sealed with a welded cap for shipment.

The closure head is secured to the RPV with 26 closure stud assemblies, which pass through the bolting flanges of both the head and the vessel. Each stud is 5.732 in. in diameter and 108.5 in. long and is retained by extension nuts having spherical ends seated on matched spherical washers. The stud assemblies (stud, nuts, washers) are fabricated from ASTM A-540-7, Grade B23 material.

The support flange, which is essentially a 19-in. thick spacer ring positioned between the bolting flanges of the RPV and closure head, is part of the upper core barrel. The flange is fabricated from a forging of ASTM-A508, Class 4, low-alloy steel. The support flange is welded to the upper core barrel. The alignment keys that match the closure head and support flange were not reinstalled during package preparation.

The RPV internals include the thermal shield, filler plates and core barrel. These components, as well as the RPV wall, are radioactive. In addition, other radioactive steel components were loaded into Vandenburgh liners and placed with the RPV. The total radioactivity is estimated to be 16,000 ± 3000 Ci by WHC. The RPV/NST package is classified as a Category II package as indicated in Section 1.2. The radioactive contents are nondispersible (i.e. remain well below the radioactive material release limits

for accident conditions). Also, the radioactivity was caused by neutron activation and is interspersed over a large volume in components such as the core barrel. Significant radiation shielding is provided primarily by the RPV's thick-wall. The external radiation levels can increase significantly only if the RPV/NST package fails catastrophically and allows large components such as the core barrel to become exposed.

2.2 Material Properties

2.2.1 General

Primarily, concrete and steel materials are used in the construction of the RPV/NST package. The steel provides structural strength; the NST outer shell confines the package radioactive contents; and the RPV wall provides radiation shielding. The concrete provides additional shielding of the radioactive contents, holds the various parts of the RPV/NST in position to form an integral monolithic solid package, and acts as an energy-absorbing material under normal and hypothetical accidental impact conditions.

The type of material properties required for analyzing the RPV/NST package depend on the computer model used in the analysis. All analyses were performed with the LLNL computer codes DYNA 2D/3D (DYNA). The materials used in the analyses are steels, concrete, and insulation. The steels in the RPV/NST package are represented by the DYNA kinematic/isotropic elastic-plastic (Type 3) material. The concrete is represented by the pseudo-tensor concrete/geological model (Type 16) material. The vessel insulation is represented by the soil and crushable foam (Type 5) material. Appropriate properties were identified for each of the RPV/NST materials as required for the three different DYNA types of materials. The material properties used in the analyses are given in the following subsections for steel, concrete, and insulation.

2.2.2 Steel

The DYNA Type 3 material requires these properties to be input for each steel used: density (ρ), Youngs Modulus (E), Poisson's ratio (υ) yield

stress (σ_y), hardening modulus (E_t), and hardening parameter (β). Since these property values are approximately the same for NST/RPV steels, these values were input: $\rho = 0.28$ lb/in^3, $E = 30 \times 10^6$ psi, $\nu = 0.30$, and $\beta = 1$. The other material properties were based on information mostly supplied by WHC as summarized in Table 2-1.

The hardening modulus can be calculated as follows:

$$E_t = \frac{\sigma_u - \sigma_y}{\varepsilon_u - \varepsilon_y}$$

where stresses (σ_u and σ_y) and strains (ε_u and ε_y) are the true stresses and true strains corresponding to the ultimate and yield points of an engineering tensile stress-strain curve.

Room-temperature properties were used in all cases. All steels were modeled to have unlimited strain-hardening capability.

2.2.3 Concrete

2.2.3.1 Formulation

Two different formulations were used for the concrete fill in the RPV/NST package as shown in Tables 2-2 and 2-3. Both formulations are grout-like because sand is used as the aggregate. Both concretes were formulated to be lightweight, have good flowability, and have a low heat of hydration. The concrete in the RPV is formulated to be slightly expansive to insure that the components and Vandenburgh liners in the RPV are firmly fixed in place. The concrete in the NST region is formulated to have essentially zero expansion and little or no shrinkage.

To reduce the heat of hydration, Type II Portland cement is used for massive concrete structures or where the concrete structural member is very thick. With ordinary cement, the heat generated in the grout could cause unknown stresses in the plates and shells of this package. Type II cement reduces the temperature rise in the grout.

Flyash plays multiple roles in concrete. It is light weight. In the presence of cement, it has cementitious properties, and hence it is used as a partial replacement of cement for economy. It helps reduce the heat of hydration of large masses of concrete. It also reduces the shrinkage of concrete.

Sand, a fine aggregate, fills the voids between the coarse aggregates in an ordinary concrete. In the grout mix, sand is used as an aggregate for strength, volume, and ease in pumpability.

Intraplast-M is an admixture that imparts two very desirable properties, namely, flowability and a slight gaseous expansion in the grout mix. With this ingredient, the grout easily flows to hard-to-reach places, even with less water, and its expansive property forces the grout into close contact with the surrounding surfaces. Without this expansive property, there would be a gap between the vessel and the grout when the latter shrinks. Because the expansion of the grout could cause extra stresses in the vessel, the quantity of the intraplast-M was adjusted so that it prevents shrinkage but does not create undesirable expansion at the same time. The concrete fill was poured in several lifts to reduce temperature build-up in the package and to preclude thermal expansion.

Water not only makes a mix plastic but also controls the strength of the hardened concrete. The water-to-cement ratio (W/C) by weight has a definite relationship with the strength. Therefore, the quantity of water is predetermined for a given strength. In the present case, a certain portion of flyash would also participate as cement, and hence the quantity of water was adjusted to take this participation into account. If there were no flyash a W/C of 0.795 would cause the strength of the grout to be 2500 psi. However, with 1/3 flyash acting as cement, W/(C+F) is 0.6, and predicted strength is 3800 psi at 28 days.

2.2.3.2 Material Type 16 in DYNA

Material Type 16, the pseudo-tensor concrete/geologic model, was chosen for use in DYNA because this material type has softening and confinement

accounted for in the coding. Material type 16 has a "default" input set that is based on common concrete and requires only the compressive strength of the concrete to be specified. However, because the concrete in the Shippingport package is a grout without large aggregate and uses large amount of flyash, more than the compressive strength is required in the analysis to model the concrete in this package.

In order to model concrete, several property values such as the shear modulus (G), Poisson's ratio (ν), tensile cut-off stress (sigf), cohesion (a_0), and pressure hardening coefficients (a_1 and a_2) are needed in simulating concrete behavior with Material Type 16. The Stanford Research Institute (SRI) was contracted to measure the required properties. The NST concrete must not only hold components in place, but must also act as an energy absorber and prevent excessive deformation of the NST outer shell. Test samples using the NST concrete formulation in Table 2-3 were prepared by Construction Engineering at the Shippingport site under the direction and quality assurance program of General Electric. The samples were prepared from a full truckload batch size to simulate what would be used to fill the NST vessel. The samples were 4 inches in height and 2 inches in diameter.

The material tests at SRI were conducted under a quality-assurance program and an approved test plan after the concrete had cured for approximately 42 days. The main tests that SRI conducted were the confined triaxial tests, which have confining pressures of 0, 2, 4, and 8 ksi. The load path in each of these tests starts with equal axial and radial loads (a hydrostatic loading condition) up to the specified confining pressure for that test. Then, the axial load is further increased beyond this specified confining pressure while the radial load is maintained at this confining pressure. The test with zero confining pressure is a special case, which corresponds to the standard concrete test for compressive strength. A complete description of these tests and results can be found in Ref. 6. The material properties measured by SRI for the NST concrete are summarized in Table 2-4.

The RPV/NST package is scheduled to be shipped about 11 months after the initial pour of concrete into the annulus between the outer shell and the RPV. WHC conducted compressive strength tests on the formulated concrete up to 42 days of curing. For these samples, WHC used the NST concrete formulation. The results are shown in Figure 2-2. Five compression tests performed by SRI with the Construction Engineering samples fall in a narrow range. The average compressive strength was 4200 psi at 44 days. SRI also tested three WHC samples at 58 days and measured an average compressive strength of 5000 psi. Later, seven samples from the actual NST pour were tested at SRI and had an average compressive strength of 4800 psi at 62 days. The ranges of these three sets of additional tests by SRI are also shown in Figure 2-2. From these results, the projection of compressive strength to the time of shipment can be made. The projected compressive strength of 6400 psi at 260 days as shown in Figure 2-2 is used to scale the SRI results by a factor of 1.52 (6400/4200) to correspond to a cured age of approximately 11 months. It is important to point out that the rate of increase in concrete strength is not significant beyond a few months after the pour.

2.2.4 Insulation Material

The soil and crushable foam model (material type 5) is used with DYNA2D/3D to represent the insulation. The input for this model includes the following information: parameters describing pre-yield stress and post-yield behavior, bulk unloading modulus k, and a pressure-vs-volumetric strain curve for the material. Since the insulation has virtually no elastic strength, the yield strength is to be 1.7 psi, and an elastic shear modulus of 1.0 psi is input. The pressure vs volumetric strain data is given in Table 2-5. The bulk unloading modulus used is 1.481×10^4 psi.

Table 2-1 Mechanical properties of steels used in the Shippingport package.

Material	Package component	Yield strength (ksi)	Tensile strength (ksi)	Elongation (%)	Notes
ASTM-A508-67, Class 4	Reactor closure head	85	105	18	a
ASTM-A540-7, Grade B23	Closure studs	100	115	10	b
ASTM-A508, Class 4	RPV support flange	85	105	18	a
ASME-SA212, Grade B	NST shell & head	38	70	18	c
ASME-SA201, Grade B	NST cone & ring girder	45	90	40	d
ASTM-A7 or ASTM-A36	NST structural steel	36	58	20	e
ASTM-A302, Grade B	RPV plates & nozzles	72	93	26	f
ASTM-A182	RPV flange	66	88	25	g
Stainless Type 304	RPV nozzles (thinner section)	36	74	85	h

a Telecopy from WHC to LLNL dated 11-06-87.
b Telecopy from WHC to LLNL dated 11-06-87.
c ASTM Tentative Specification (A212-61T).
d Same as ASTM SA-412 according to Unified Numbering System.
e A7 is now obsolete and has been supplanted by A36.
f Testing by Lukens Steel Company for Combustion Engineering Company.
g Testing by Bethlehem Steel Company for Combustion Engineering Company.
h Testing by Lukens Steel Company for Combustion Engineering Company.

Table 2-2 Lightweight grout for the RPV cavity.

Materials	Batch weight (lb)
Cement (Medusa Type II)	2345
Flyash	2325
Fine aggregate (sand) dry	4220
Fluidifier (intraplast)	46
Minimum water to meet flowability requirement	

Properties	
Flowability (CRD - C611)	25 - 35 sec
Compressive strength (ASTM C39-86)	>2000 psi
Density (ASTM C567-85)	100 - 130 lb/ft^3
Shrinkage/expansion (CRDC-621-83)	+.2% to -0% max

Table 2-3 Lightweight grout for the NST and skirt.

Materials	Batch weight (lb) per cubic yard
Cement (Medusa Type II)	746
Flyash	746
Fine aggregate (sand) dry	1243
Fluidifier (intraplast)	5
Total allowable water	593

Properties	
Flowability (CRD - C611)	20 - 35 sec
Compressive strength (ASTM C39-86)	>2000
Density (ASTM C567-85)	100 - 130 lb/ft^3
Shrinkage/expansion (CRDC-621-83)	+0.005% to -1.00% max

Table 2-4 Mechanical properties and DYNA3D material 16 parameters of concrete grout at 42 days after initial pour.

1. Compressive strength (f_c') = 4.24 ksi
2. Modulus of elasticity (E) = 2170 ksi
3. Density (ρ) = 125.2 lb/ft^3
4. Poisson's ratio (ν) = 0.22
5. Shear modulus (G) = 950 ksi
6. Tensile cutoff stress (sigf) = 0.87 ksi
7. Cohesion (a_0) = 11.2 ksi*
8. Pressure hardening coefficient (a_1) = 6.06 ksi*
9. Pressure hardening coefficient (a_2) = 0.0 ksi*

* Values derived for a linear fit to the SRI data at 42 days of curing. A polynomial fit was used in the final analysis.

Table 2-5 Pressure and volumetric strain properties for Shippingport RPV insulation.

Pressure (psi)	Volumetric Strain
0	0
3.7×10^{2}	-2.5×10^{-2}
6.2×10^{2}	-6.9×10^{-1}
1.2×10^{3}	-9.8×10^{-1}
3.8×10^{3}	-1.4

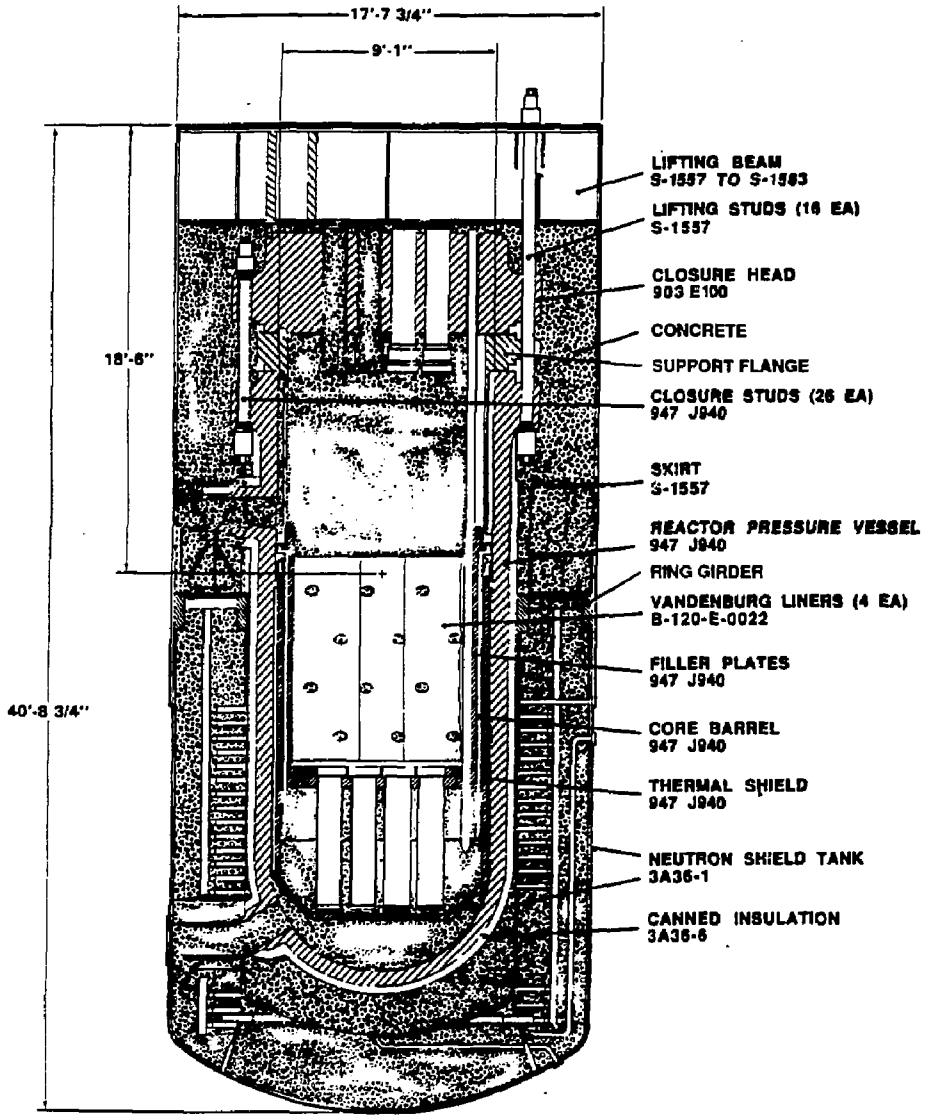

Figure 2-1 Cutaway of the Shippingport RPV/NST package.

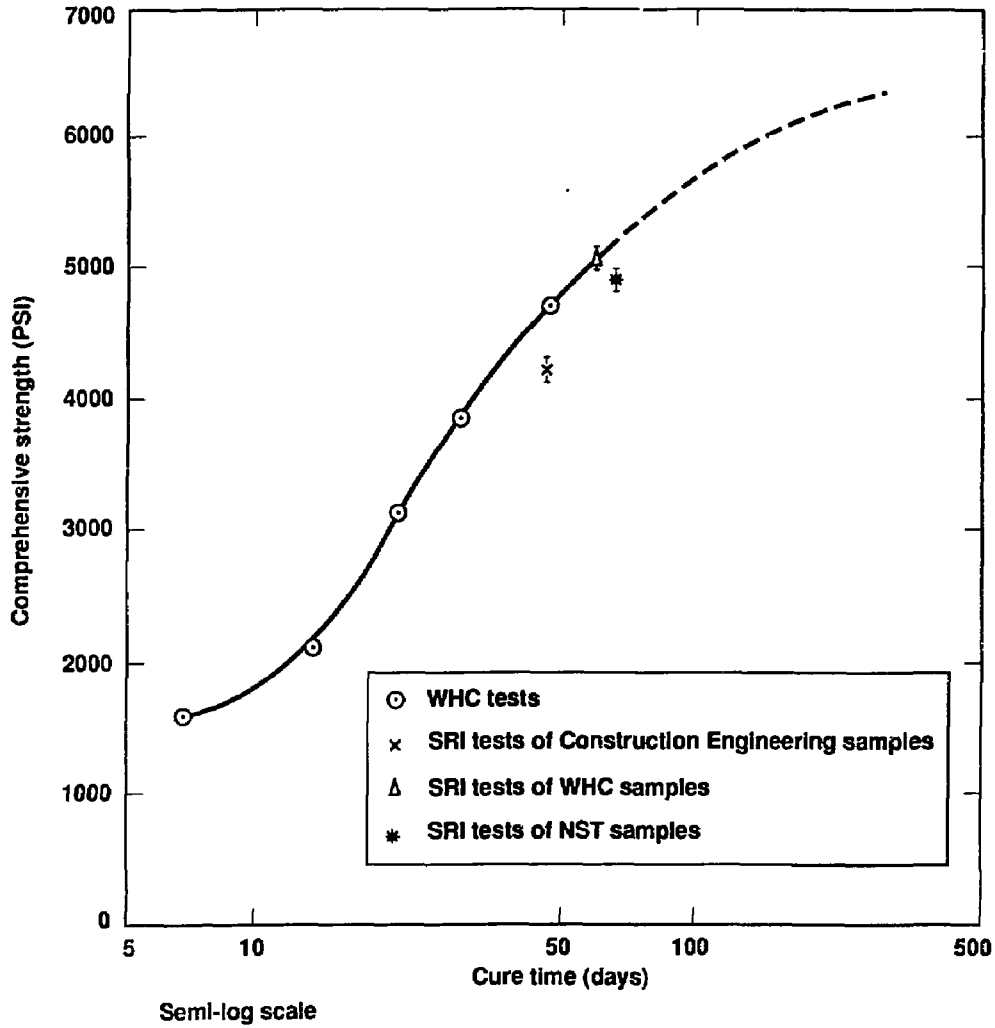

Figure 2-2 Compressive strength of NST fill concrete as function of cure time.

3.0 Benchmark of Analytical Approach Used in Structural Evaluation

3.1 Introduction

A benchmark study combining tests and finite element analyses was performed. The purpose of the benchmark tests were to demonstrate that results of the structural analyses of the package using the DYNA codes are a reasonable representation of its real structural behavior. The general approach for performing the benchmark validation was to analyze the structural response of test specimens and then compare these results with the actual experimental drop tests.

3.2 Benchmark Specimen

Before benchmark testing of DYNA could be performed, the benchmark specimen configurations and drop heights had to be defined. The benchmark specimen had to have all the major significant geometric characteristics of the RPV/NST package and had to use the same concrete as in the NST fill of the package. In addition, the benchmark testing had to be designed such that all significant structural and dynamic parameters would be tested at least over the ranges that apply to the RPV/NST package. For example, the deformation of the outer NST shell was important. The benchmark testing had to be planned such that the expected level of deformation of the NST shell would be reached in the benchmark experimental test.

Sensitivity studies were performed with DYNA analytical models to establish the benchmark specimen configuration and test drop heights. All experimental tests were planned to be performed using an "unyielding" drop pad. In the following two subsections the sensitivity study performed is discussed and the benchmark specimen configuration selected is described.

3.2.1 Sensitivity Scoping Study

Full size, 1/10 and 1/100 size models of the RPV/NST were analyzed for a 30 foot drop onto an unyielding surface. The results of the analyses for drops onto the round end are compared with the full scale RPV/NST analysis.

The 1/10 size was selected for performing the experimental benchmark tests. This size is large enough to relate dynamic and structural responses (including instrumentation) to the RPV/NST package and to use fabrication methods similar to those used for the RPV/NST package but yet small enough to test on existing drop pads.

3.2.2 Description of the Test Specimen

The major components of the selected benchmark test specimen shown in Figure 3-1 are an inner vessel which simulates the RPV, an outer container which simulates the NST, and a concrete fill material which is the NST formulation in Table 2-3. The inner vessel is constructed from steel pipe (schedule 80, ASTM A53) with a seamless weld cap at the lower end, and steel plates (ASTM A36) at the upper end. The total length and diameter of the inner vessel is 37.6 inches and 12.75 inches respectively. The outer container is fabricated from rolled steel plates (ASTM A569) welded to form a cylinder, with a tank head on the lower end and a flat steel plate (ASTM A569) at the upper end. The total length and diameter of the outer container is 51.6 inches and 22.0 inches respectively. The weight of each specimen is about 1820 pounds.

3.3 Finite Element Analysis of the Benchmark Test

Two analytical models were generated according to the description of the test specimen. One is a two dimensional finite element model for the DYNA2D analysis of end drops which take advantage of loading and geometric symmetry. The other is a three dimensional model for the DYNA3D analysis of side drops and corner drops.

Both benchmark analytical models used the DYNA material type 16 to model the concrete. Based on tests performed by WHC and SRI as previously presented in Figure 2-2 the expected compressive strength of the concrete is approximately 3850-4240 psi during the testing period from 28-35 days after filling the specimen with concrete. The compressive strength of 4240 psi was used in all benchmark analyses which is the average value measured by SRI in

defining the material type 16 properties at 44 days. The benchmark analyses used all the material type 16 properties measured at SRI. No change in these values were required because the same compressive strength was used.

Both benchmark analytical models used the DYNA material type 3 to model the steel components. The material properties used in the benchmark analyses for each of the steels are listed in Table 3-1.

3.3.1 Two-Dimensional Analytical Model of the Benchmark Specimen

The two-dimensional (2-D) analytical model of the Shippingport benchmark test specimen was generated using the finite element mesh generator code SLIC (Ref. 7). The 2-D benchmark model assumes axisymmetric behavior along the length of the cylindrical package. This benchmark model is composed of concrete surrounding the vessel, concrete inside the vessel, the head piece, the vessel, and the outer shell. The shell/concrete interface is modeled as a frictionless contact surface which allows the shell to separate from the concrete. An exploded view of the 2-D benchmark model is shown in Figure 3-2. The details of this finite element model are summarized in Table 3-2.

3.3.2 Three-Dimensional Analytical Model of the Benchmark Specimen

The 3-D benchmark model is composed of concrete surrounding the vessel, concrete inside the vessel, the vessel, the head piece, and the outer shell. The shell/concrete interface is modeled as a frictionless contact surface which allows the shell to separate from the concrete. An exploded view of this 3-D benchmark model is shown in Figure 3-3. This model was also generated using the finite element mesh generator SLIC. Table 3-3 summarizes this benchmark finite element analysis model of the Shippingport package.

3.4 Benchmark Experimental Tests

The benchmark drop tests were conducted by WHC at a drop facility furnished by Battelle Pacific Northwest Laboratories (PNL). The tests, conducted in late February and early March, 1988, were performed in accordance with the WHC test plan (Ref. 8). Eleven drop tests were performed on seven

specimens shown as a test matrix in Table 3-4. Test specimens (1, 2, 3, and 6) were dropped twice, whereas the rest were only dropped once. There were eight drops from 30 feet, two from 45 feet and one from 1 foot. WHC provided LLNL the test results for comparison with those from nonlinear finite element analysis using DYNA codes (Ref. 9).

3.5 Test and Analyses Comparison

The fundamental comparison to be made between the benchmark experimental test results and the analytical predictions are deceleration and gross outer shell deformations after impact. It was anticipated that gross deformation would be measured directly for comparison with analytical results. Experimental decelerations were measured using triaxial piezo-electric accelerometers mounted on the vessel simulating the RPV.

3.5.1 Decelerations After Impact

One measure of the validity of the analyses is a comparison of the computed deceleration time histories with the experimental time histories for the corresponding drop configuration. In both cases the data presents instantaneous values of deceleration that include higher harmonics of the impulse (ringing). These higher harmonics were removed to some extent in the test by the use of a filter in the accelerometer signal circuit. The accelerometer readings of the early test drops, 1A, 1B, and 2B were invalid because the ringing in these test specimens overloaded the charge amplifier. This problem was resolved in subsequent tests by incorporating a filter. Consequently, only test numbers 2A, 3A, 3B, 4, 5, 6A, 6B, and 7 are used for comparison of deceleration time histories.

Besides a comparison on the peak deceleration we have also compared the time interval between initial impact and the time at which the deceleration is reduced to zero. Within this time interval the bulk of the kinetic energy is dissipated. Furthermore, this time interval is indicative of the structural response of all the materials deformed in the process, since it is inversely proportional to the average impact force.

Both the computed and experimental (filtered to 2 k-hertz) time histories

are shown in Figure 3-4 to 3-23. The regions of interest in these time histories are marked on the figures. A summary of the comparison between the computed and experimental peak deceleration is shown in Table 3-5. The largest percentage difference between the computed and experimental results for all the tests is around 70%. The large disparity displayed by the side drops and flat end drops is explained by the difficulty in experimentally assuring an absolutely horizontal impact. Even small deviations from the horizontal result in large differences in deformation patterns which affect the dynamic response of the test specimens. For the end and corner drop orientations, slight variations from the angle used for the computed results have relatively little effect.

Note that, in nine out of eleven free drops, DYNA conservatively over predicts the deceleration loads or impact forces. One reason for this over prediction is that the target unyielding surface can not be achieved in real tests while DYNA has no difficulty in modeling an unyielding surface. A real target absorbs part of the impact energy. The difficulty of creating a real unyielding surface would be greater for a full size test specimen. This difficulty also points out another unrealistic and conservative aspect of applying the loading conditions of 10 CFR 71 to the Shippingport RPV/NST package.

The comparison between the computed and experimental deceleration time interval is shown in Table 3-6. The largest percentage difference between the computed and experimental results for all tests is 67%. Differences in the comparisons can be attributed to the same phenomena as previously discussed for the peak decelerations. Note that the difference for the deceleration time interval for most drops is significantly less than for the peak deceleration comparison.

3.5.2 Deformations

A second measure of the validity of the analyses is a comparison of the deformed shape of the drop test specimens with the deformed shapes predicted for the corresponding drop test configuration. The most dramatic structural deformations occur at the point of impact of the test specimens with the target plate. This was true for the round end, corner and side drops but not

for the flat end drop. For the round end and side drops the area of the "footprint" is relatively easy to estimate since it is circular for the round end drop and rectangular for the side drop. For the corner drop, the area of the footprint is irregular and its size is indicated by its largest and smallest dimension.

Figures 3-24 to 3-36 compare the computed deformations for each of the drop configurations with on-site measurements of the deformed areas. A summary of the predicted and measured deformations is shown in Table 3-7. The differences, in terms of percentages, ranged from practically zero to 28.6%. The largest difference in the deformations is associated with side drop 2B which also had a 1 foot drop and as previously pointed out, is sensitive to any deviation from absolutely horizontal impact. The only drop test where cracking occurred was the corner drop. As shown in Figure 3-32, the crack occurred in the weld region. The crack arrested which is typical of ductile rupture.

3.6 Summary and Conclusion

The purpose of the benchmark tests were to demonstrate that the results of the structural analyses of the package using DYNA codes are a reasonable representation of its real structural behavior. The two measures of the validity of the analyses used were deceleration time histories and gross outer shell deformations. Where the conditions of the drop test matched closely with those assumed for the benchmark analyses, the agreement between computed and experimented results was remarkably close. Considering the large number of variables contributed by assumed material properties, geometric idealizations of the computer model, instrument response uncertainties, testing conditions and on-site measurements, the close agreement between the experimentally measured and the calculated results, provides a large degree of confidence in the ability of the DYNA code to predict the structural behavior of the Shippingport package under normal and accident conditions.

Table 3-1 Mechanical properties of steels used in the benchmark specimen.

Material	Benchmark Specimen Component	Yield Strength (ksi)	Tensile Strength (ksi)	Elongation (%)	Notes
ASTM A36	Vessel Top Plate	36.0	58.0	20	
ASTM A53	Vessel Shell and Cap	25.0	45.0	-	a
ASTM A569	Outer Container Shell and Lid	44.2	57.9	25	b
ASTM A569	Outer Container Head	35.5	49.7	28	b

(a) ASTM minimum specification.
(b) Engineering data transmitted, RV-0009, 2 Feb. 1988, L. H. Goldman, Westinghouse Hanford Co.

Table 3-2 Two-dimensional benchmark model.

Number of Nodes: 719
Number of Elements: 611

Component	Elements/Class	Material Model
Concrete vessel	248 Solids	Pseudo TENSOR Geological Outside
Concrete vessel	130 Solids	Pseudo TENSOR Geological Inside
Head	16 Solids	Elastic-Plastic ASTM A36
Vessel	34 Solids	Elastic-Plastic ASTM A53
Outer Shell	183 Solids	Elastic-Plastic ASTM A569

Table 3-3 Three-dimensional benchmark model.

Number of Nodes:	8278
Number of Brick Elements:	5520
Number of Shell Elements:	736
Number of Thick Shell Elements:	1072

Component	Elements/Class	Material Model
Concrete Outside vessel	3456 Bricks	Pseudo TENSOR Geological
Concrete Inside vessel	1776 Bricks	Pseudo TENSOR Geological
Head	288 Bricks	Elastic-Plastic ASTM A36
Vessel	1072 Thick Shells	Elastic-Plastic ASTM A53
Outer Shell	736 Shells	Elastic-Plastic ASTM A569

Table 3-4 Test summary.

Specimen	Test No.	Orientation	Height (feet)	Declination Actual Angle (Deg.)	Degrees Desired	Drop Date (1988)
1	1A	Round End	30	86.5	90	2/24
	1B	Flat End,	30	88.5	90	2/24
2	2A	Side	1	2	0	2/24
	2B	Side	30	0	0	2/24
3	3A	Round Corner	30	61	62	2/29
	3B	Flat Corner	30	61	62	2/29
4	4	Round End	45	88.5	90	2/29
5	5	Side	45	1.0	0	2/29
6	6A	Round End	30	88.5	90	3/1
	6B	Flat End	30	88.5	90	3/1
7	7	Side	30	0.5	0	3/2

Table 3-5 Comparison of measured peak deceleration with calculated peak deceleration.

Test No.	Test Description	Calculated Peak Deceleration (g)	Measured Peak Deceleration	% Diff.(1)
2A	1' Side Drop	452	257	+43
3A	30' Round End Corner (axial direction)	679	966	-42
	30' Round End Corner (radial direction)	397	337	+15
3B	30' Flat End Corner (axial direction)	445	429	+4
	30' Flat End Corner (radial direction)	237	226	+5
4	45' Round End	1218	1067	+12
5	45' Side Drop	4274	3002	+30
6A	30' Round End	1015	1352	-33
6B	30' Flat End (deceleration)	4506	1594	+65
	30' Flat End (acceleration after impact)	818	407	+50
7	30' Side Drop	3985	1155	+71

(1) $\%\ \text{Diff} = \dfrac{\text{Calculated Peak} - \text{Measured Peak}}{\text{Calculated Peak}} \times 100.$

Table 3-6 Comparison of measured deceleration intervals with predicted intervals.

Test No.	Descriptions	Predicted Interval ms	Measured Interval ms	% Diff.(1)
2A	1' Side drop	1.98	1.5	24.0
3A	30' Round end	4.0(2)	4.5(2)	-12.5(2)
	Corner drop	4.0(3)	3.75(3)	6.3(3)
3B	30'Flat end	7.0(2)	7.5(2)	-7.14
	Corner drop	8.0(3)	8.0(3)	0.0
4	45' Round end	3.7	3.8	-2.7
5	45' Side drop	1.44	1.09	24.3
6A	30' Round end	3.7	3.5	5.4
6B	30' flat end drop	1.27(4)	1.25(4)	1.57(4)
		0.33(5)	0.34(5)	- 3.03(5)
7	30' Side drop	1.5	2.5	-67.0

(1) $\%\ \text{diff} = \frac{\text{Predicted interval - measured interval}}{\text{Predicted interval}} \times 100$

(2) Axial direction.
(3) Radial direction.
(4) Deceleration.
(5) Acceleration after impact.

Table 3-7 Comparison of measured deformations with predicted deformations.

Test No.	Description	Area of Footprint Predicted	Measured	% Diff.[1]
1A	30' Round end drop	80	80	0
2B	30' Side drop[3]	210	270	-28.6
3A	30' Round corner drop	6.0 x 11.2[2]	7.5 x10.8[2]	
3B	30' Flat corner drop	4.4 x 11.6[2]	5.5 x 17[2]	
4	45' round end drop	110	130	-18.2
5	45' side drop	310	290	6.5
6A	30' round end drop	80	85	-6.3
7	30' side drop	210	240	-14.3

(1) $\% \text{ Diff} = \frac{\text{Predicted Area} - \text{Measured Area}}{\text{Predicted Area}} \times 100.$

(2) These represent only maximum dimensions of the footprint. They cannot be used directly for computing footprint areas.

(3) this specimen was dropped twice - 1 foot and 30 foot drops.

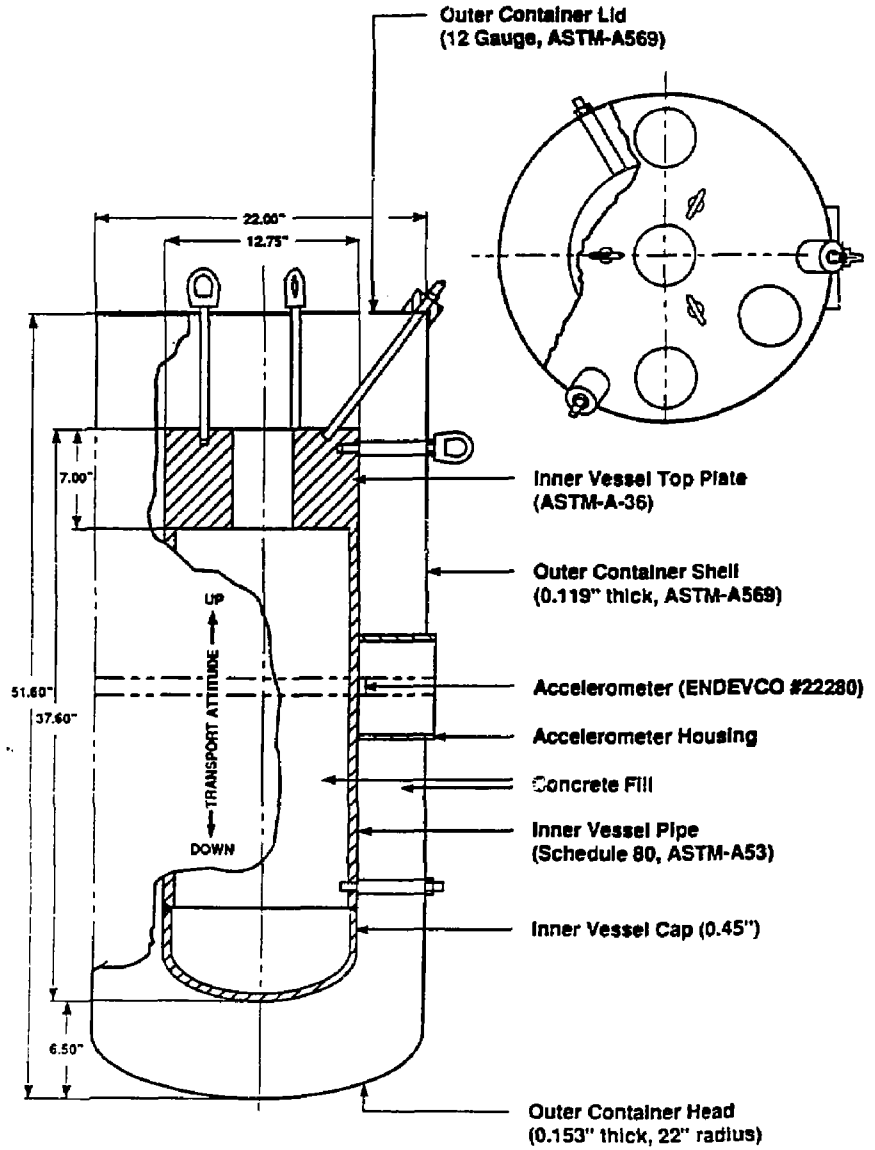

Figure 3-1 Benchmark test specimens.

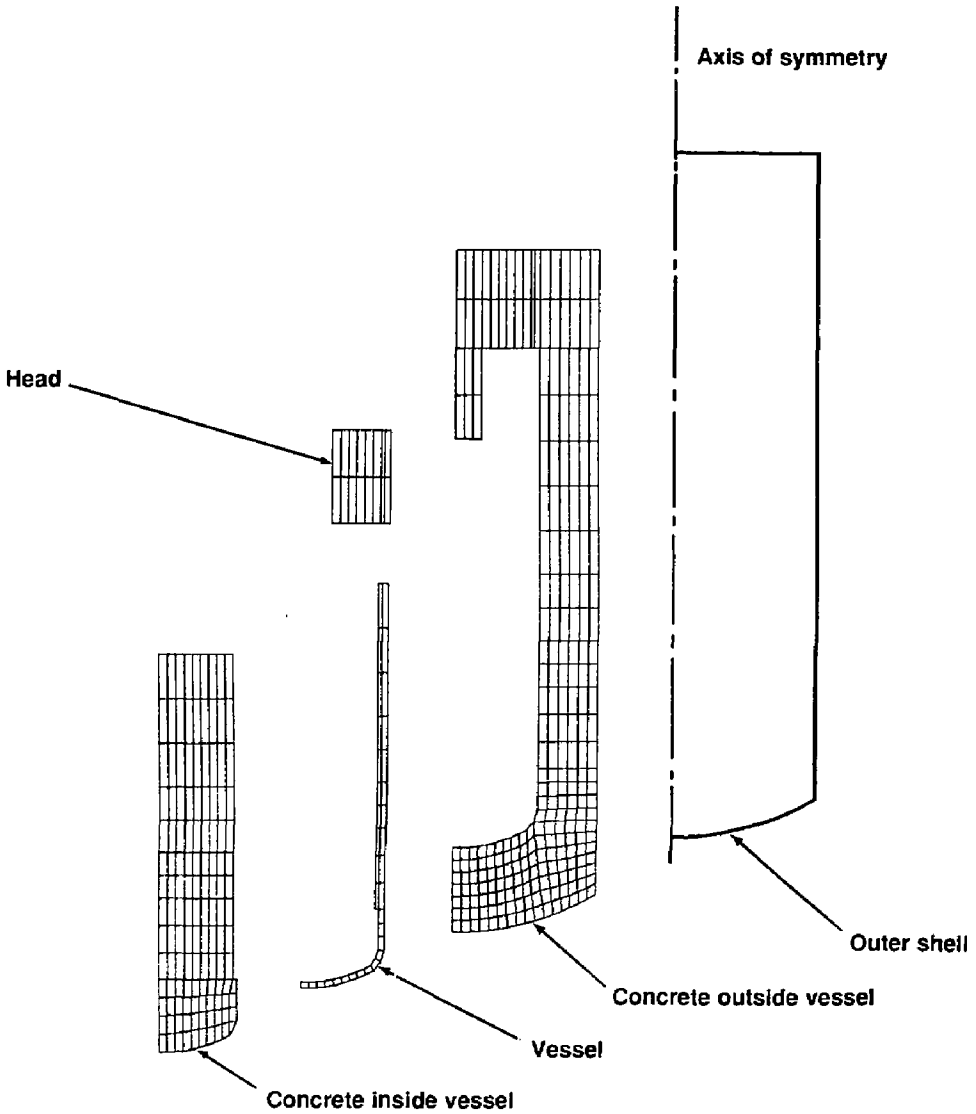

Figure 3-2 An exploded view of the 2-D benchmark analytical model.

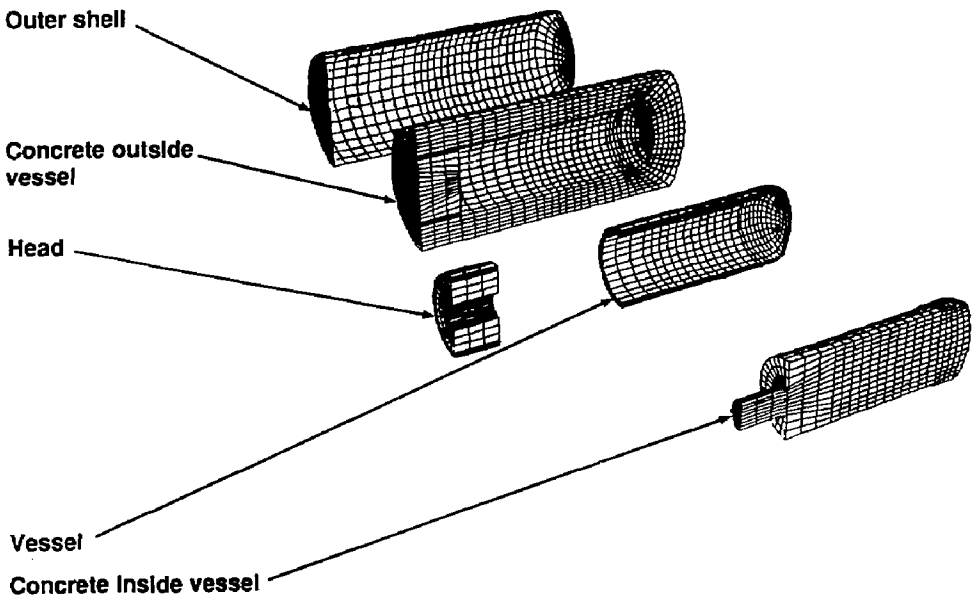

Figure 3-3 An exploded view of the 3-D benchmark analytical model.

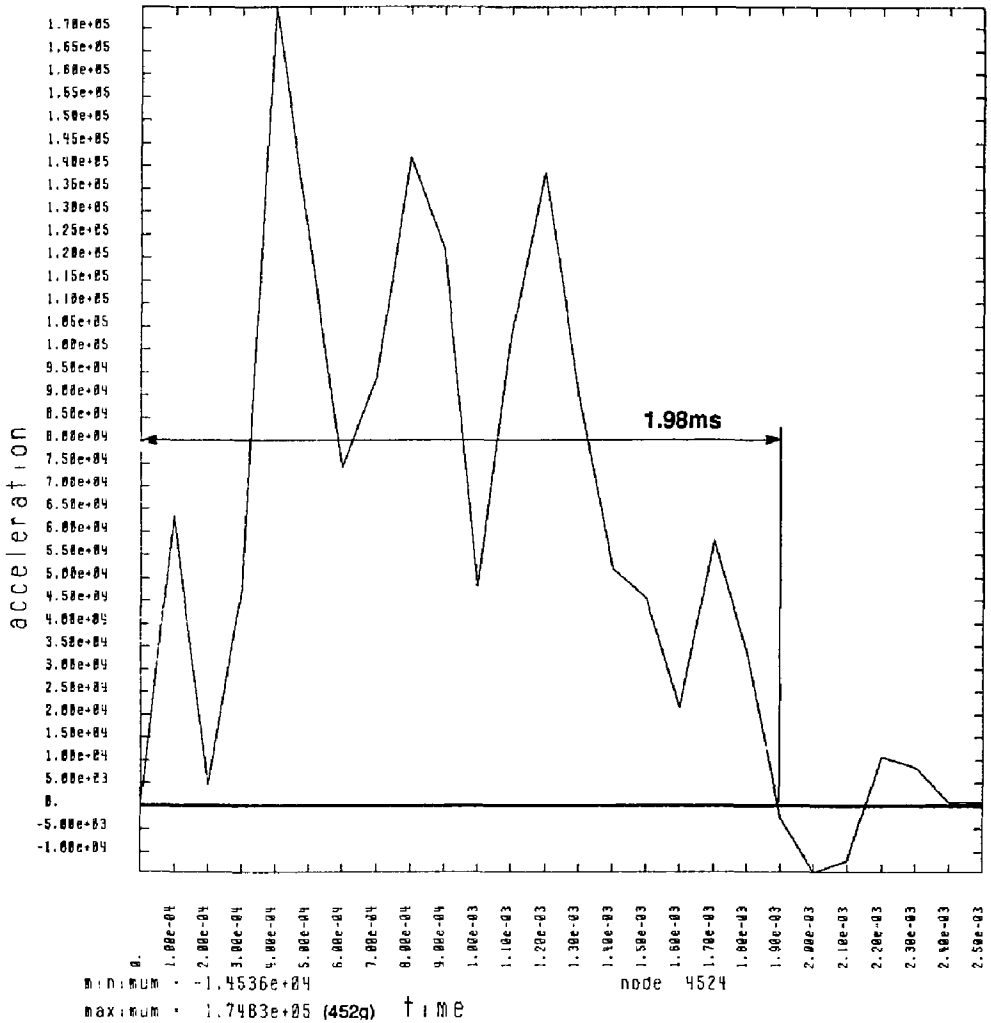

Figure 3-4 Computed deceleration time history for 1 foot side drop.

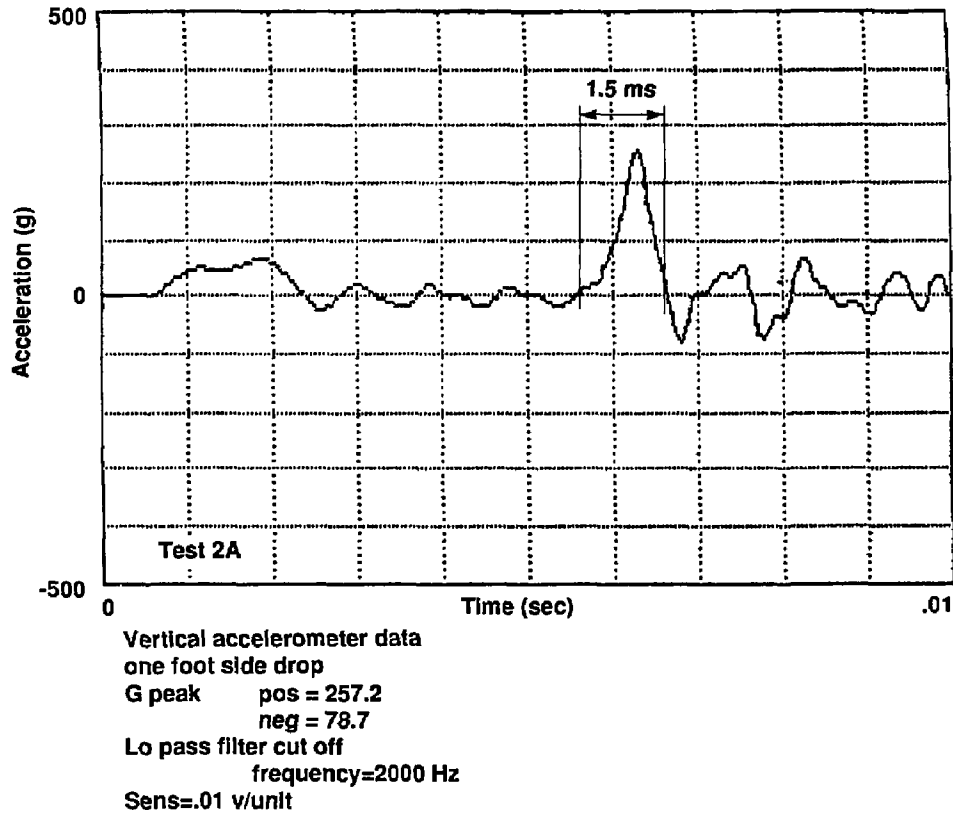

Figure 3-5 Experimental deceleration time history for 1 foot side drop.

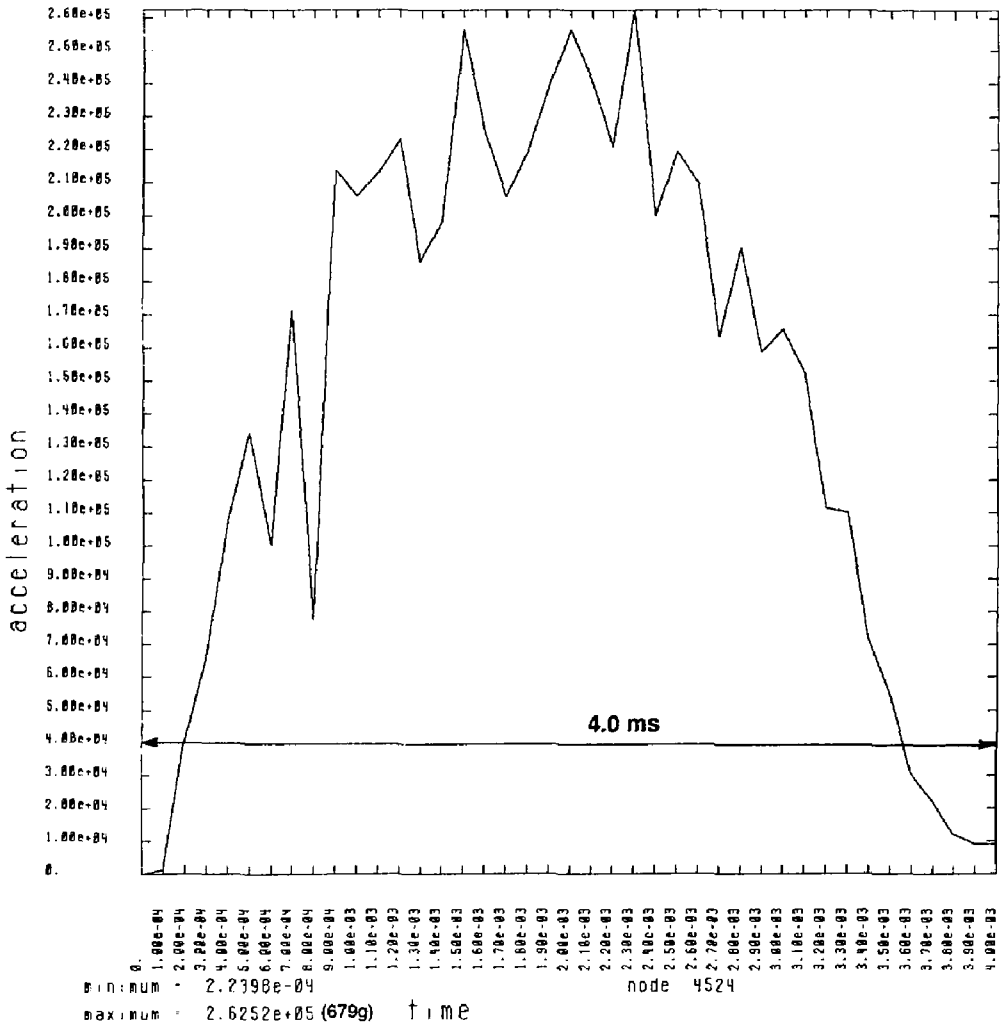

Figure 3-6 Computed deceleration time history for 30 foot round end corner drop - axial direction.

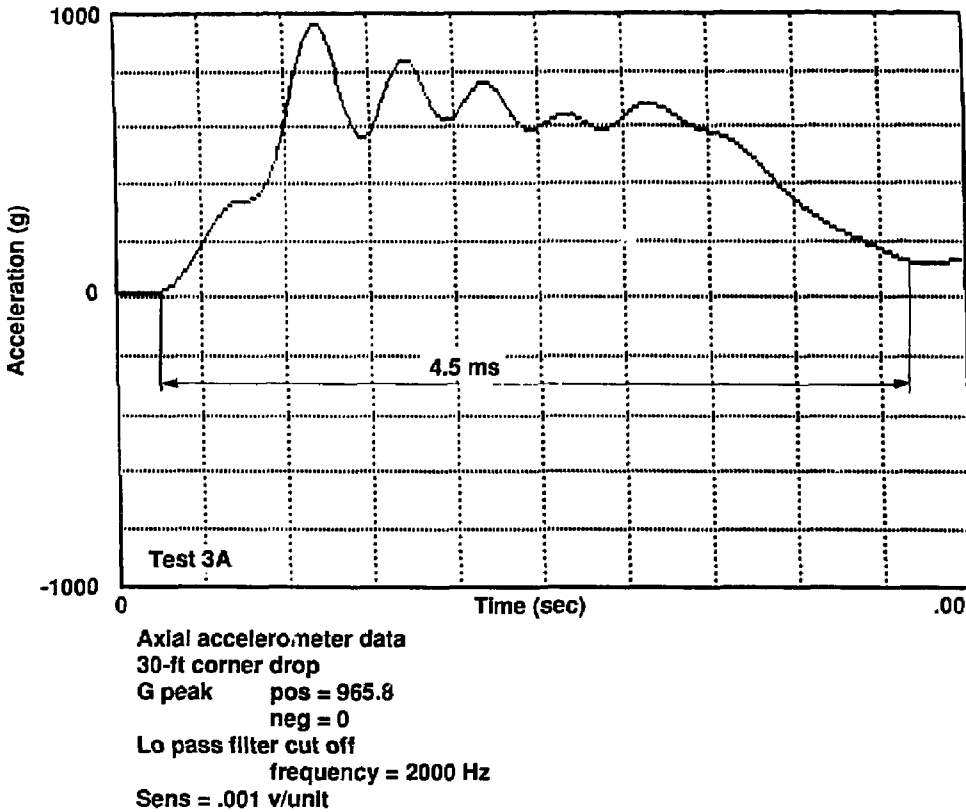

Figure 3-7 Experimental deceleration time history for 30 foot round end corner drop - axial direction.

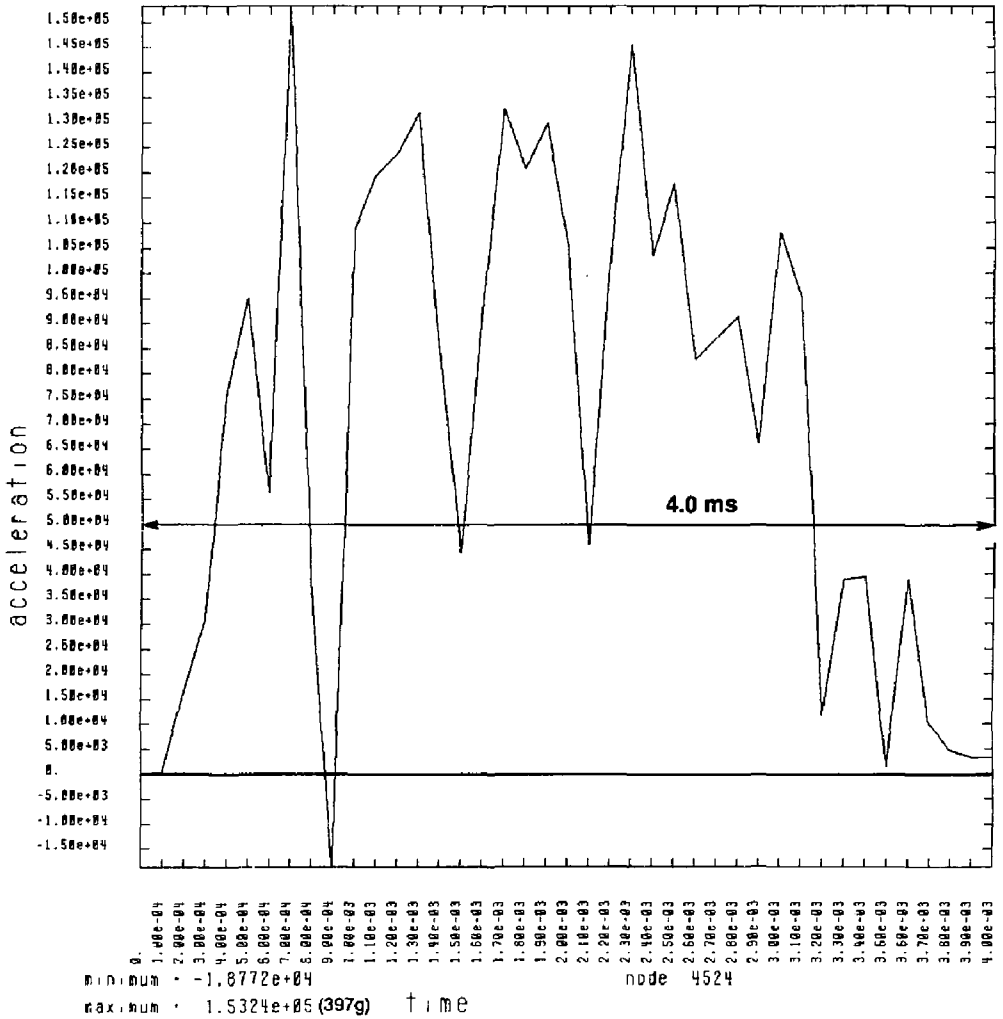

Figure 3-8 Computed deceleration time history for 30 foot round end corner drop - radial direction.

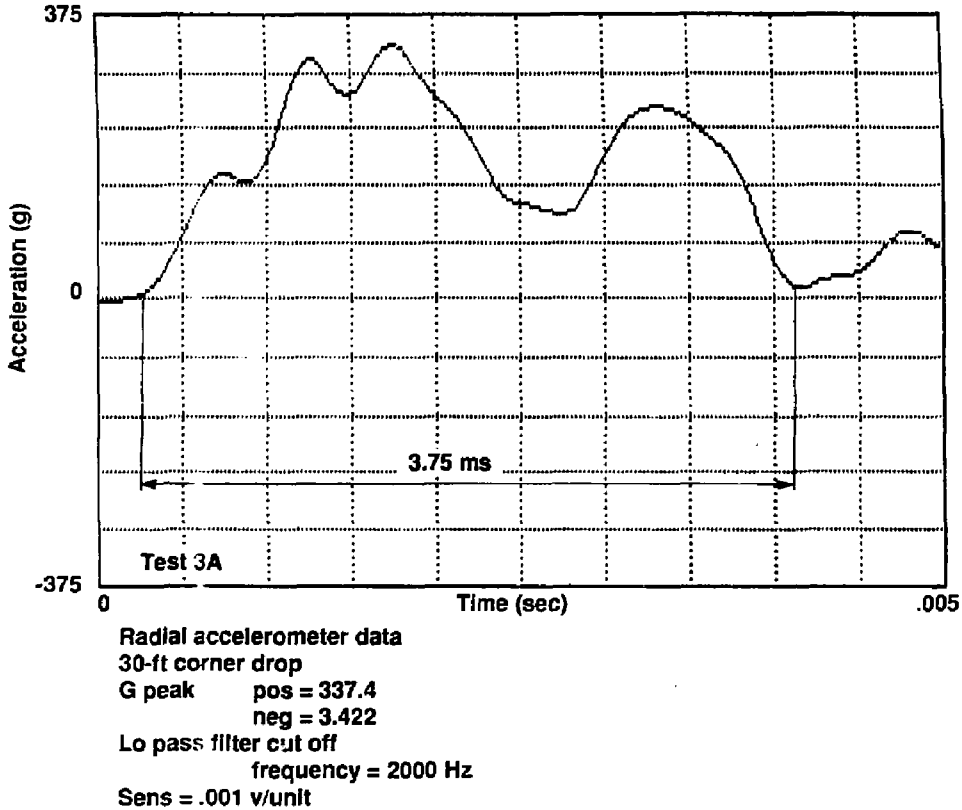

Figure 3-9 Experimental deceleration time history for 30 foot round end corner drop - radial direction.

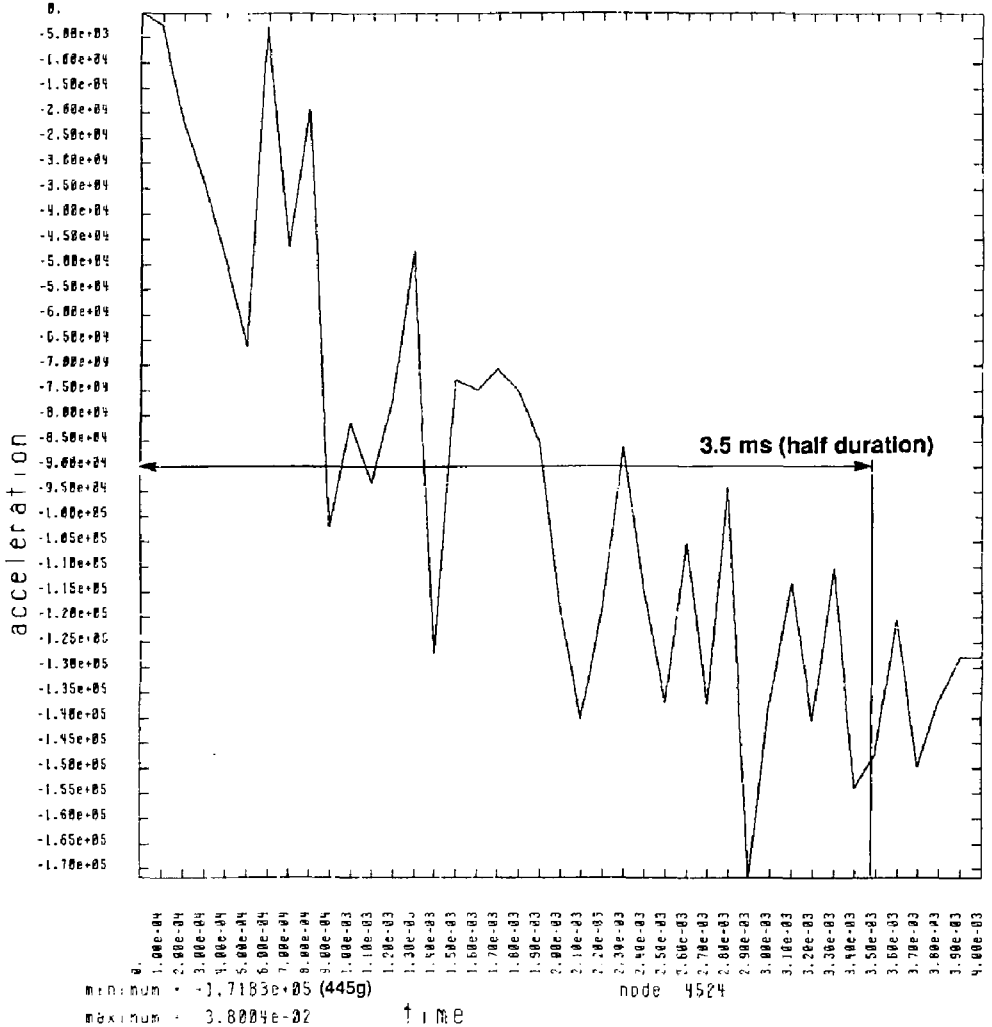

Figure 3-10 Computed deceleration time history for 30 foot flat end corner drop - axial direction.

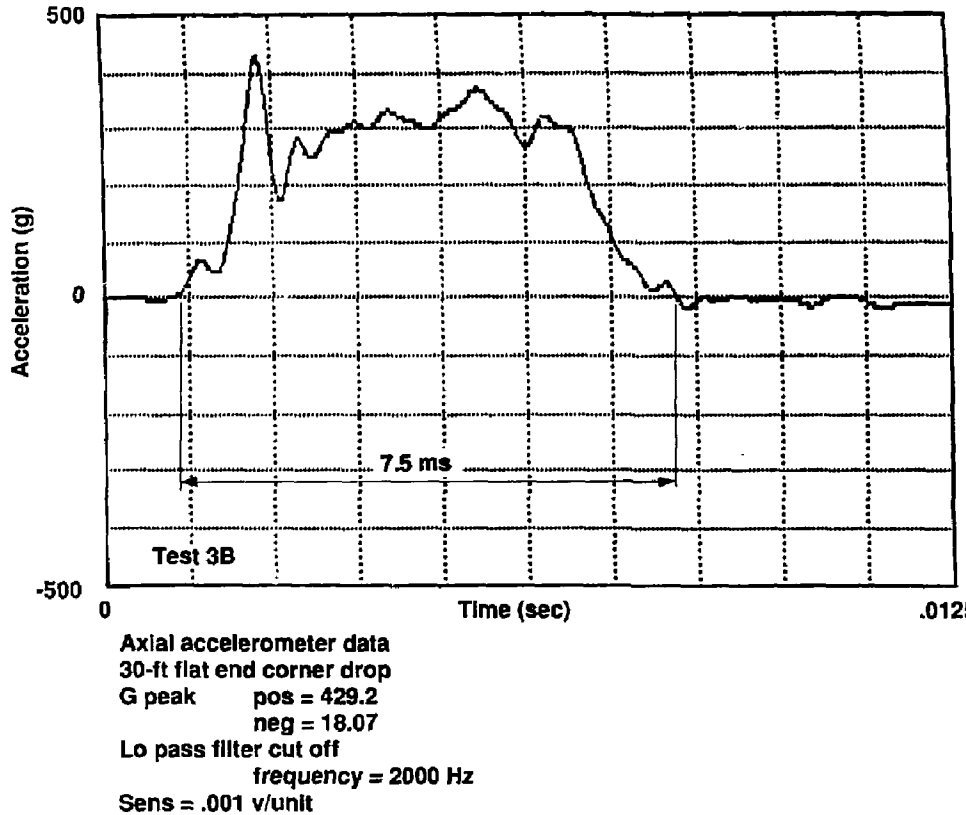

Figure 3-11 Experimental deceleration time history for 30 foot flat end drop - axial direction.

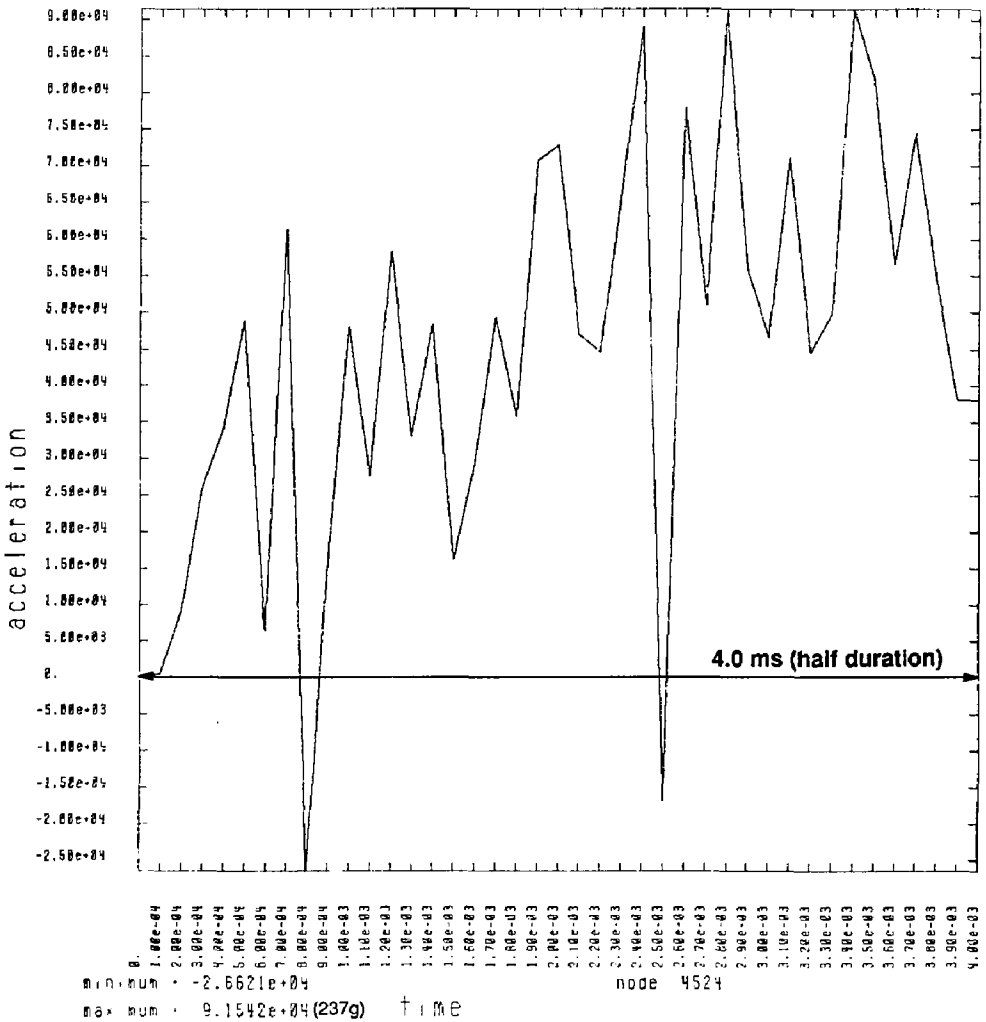

Figure 3-12 Computed deceleration time history for 30 foot flat end corner drop - radial direction.

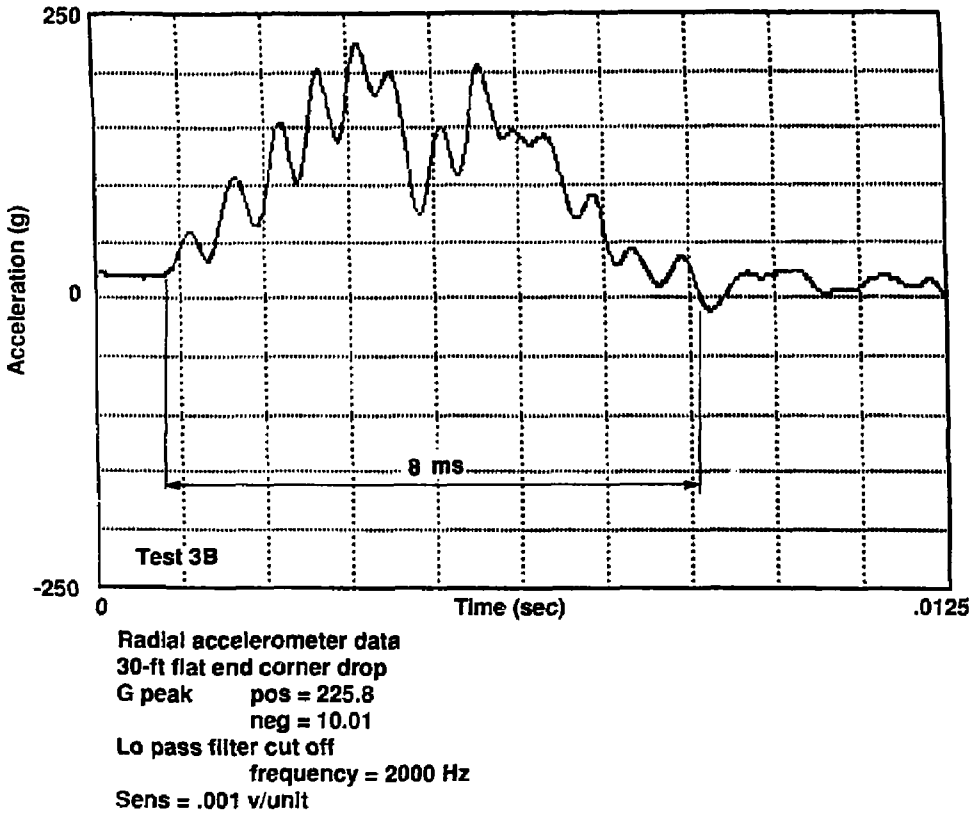

Figure 3-13 Experimental deceleration time history for 30 foot flat end corner drop - radial direction.

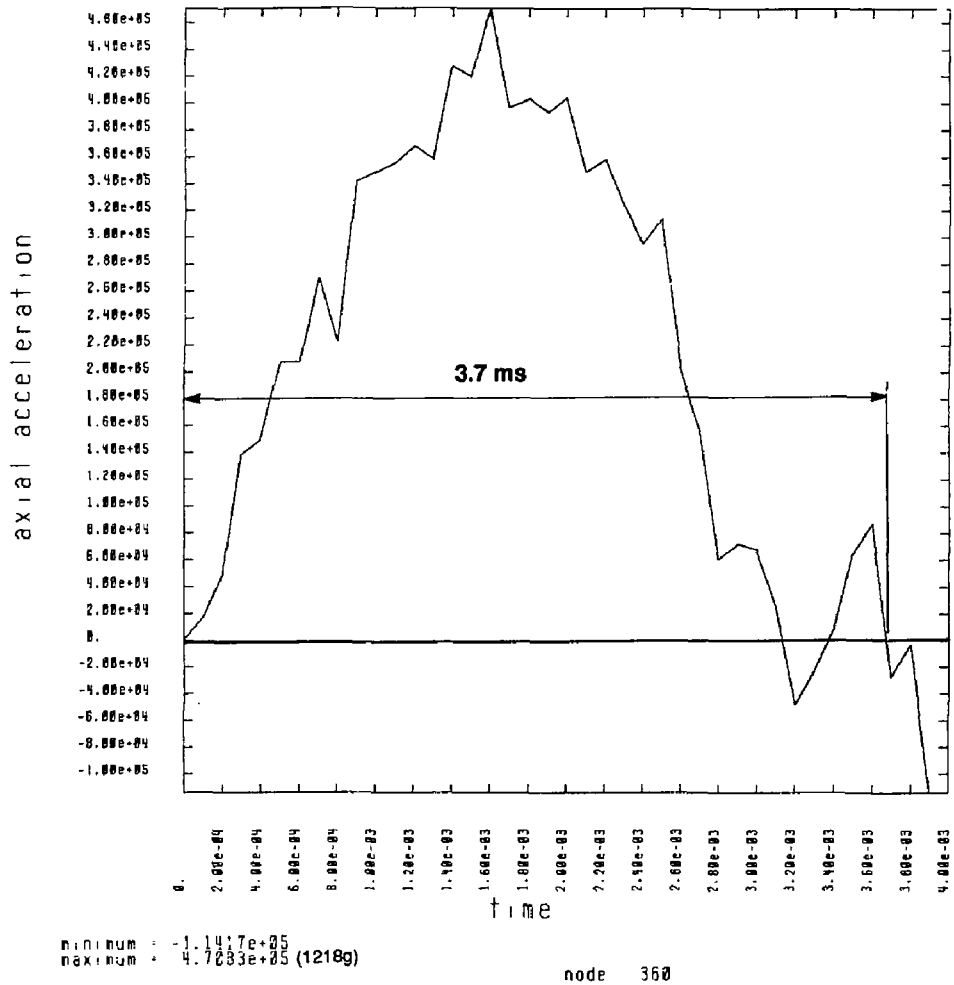

Figure 3-14 Computed deceleration time history for 45 foot round end drop.

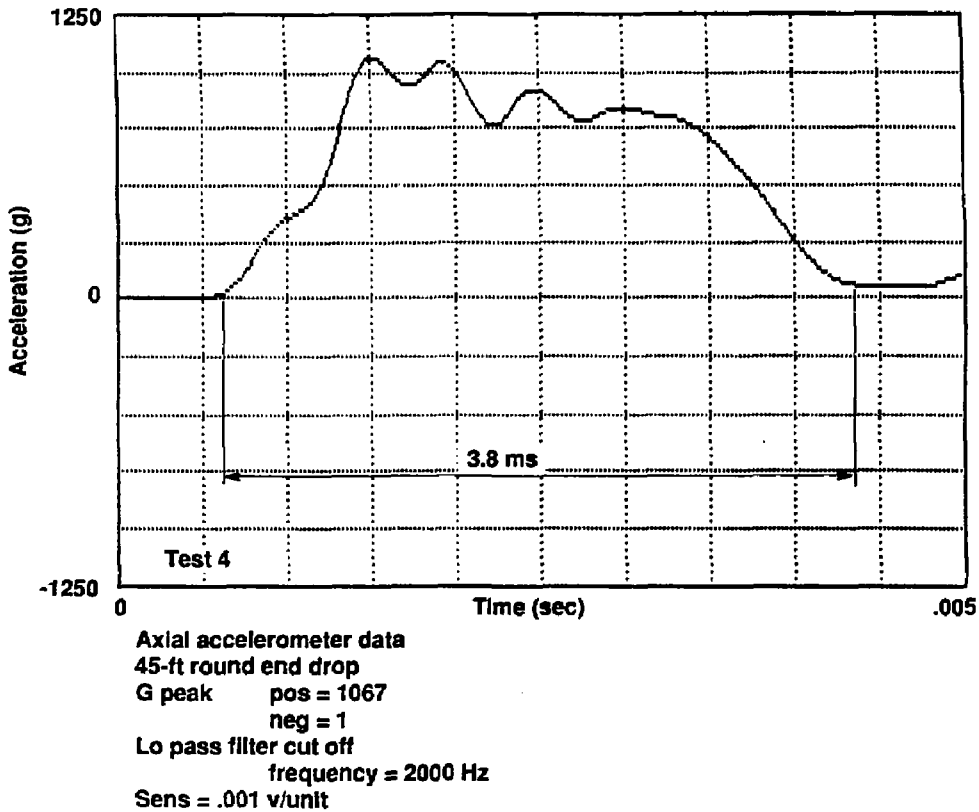

Figure 3-15 Experimental deceleration time history for 45 foot round end drop.

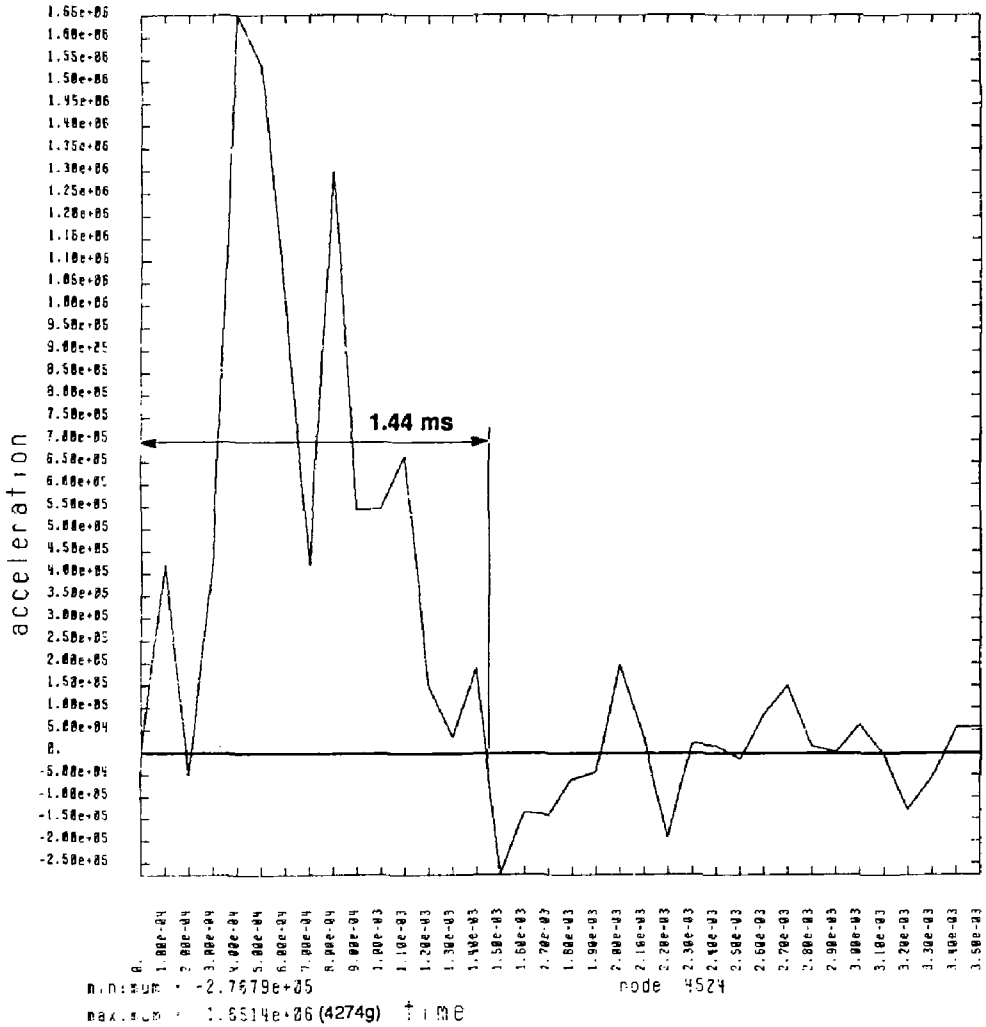

Figure 3-16 Computed deceleration time history for 45 foot side drop.

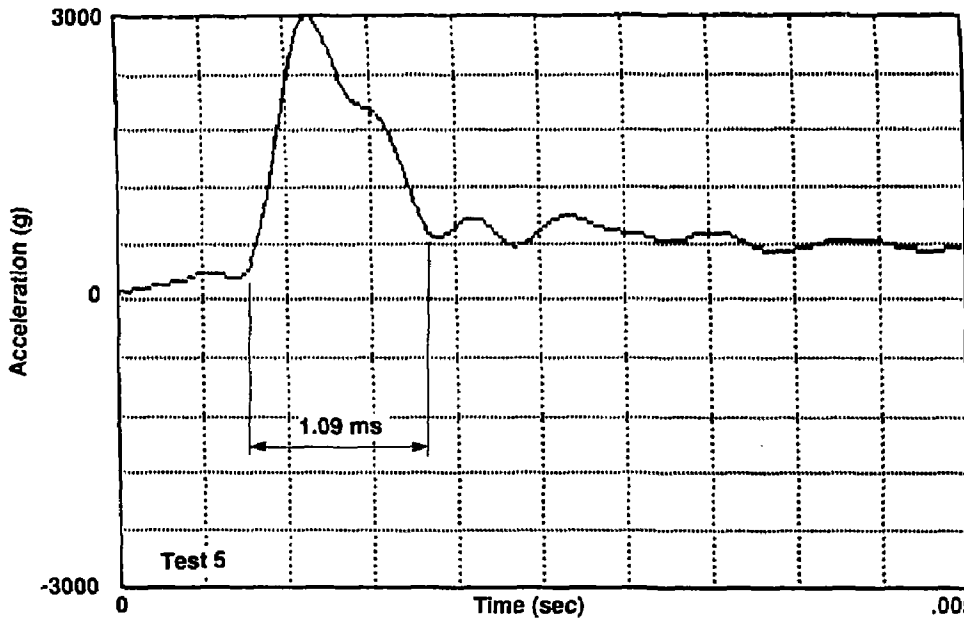

Figure 3-17 Experimental deceleration time history for 45 foot side drop.

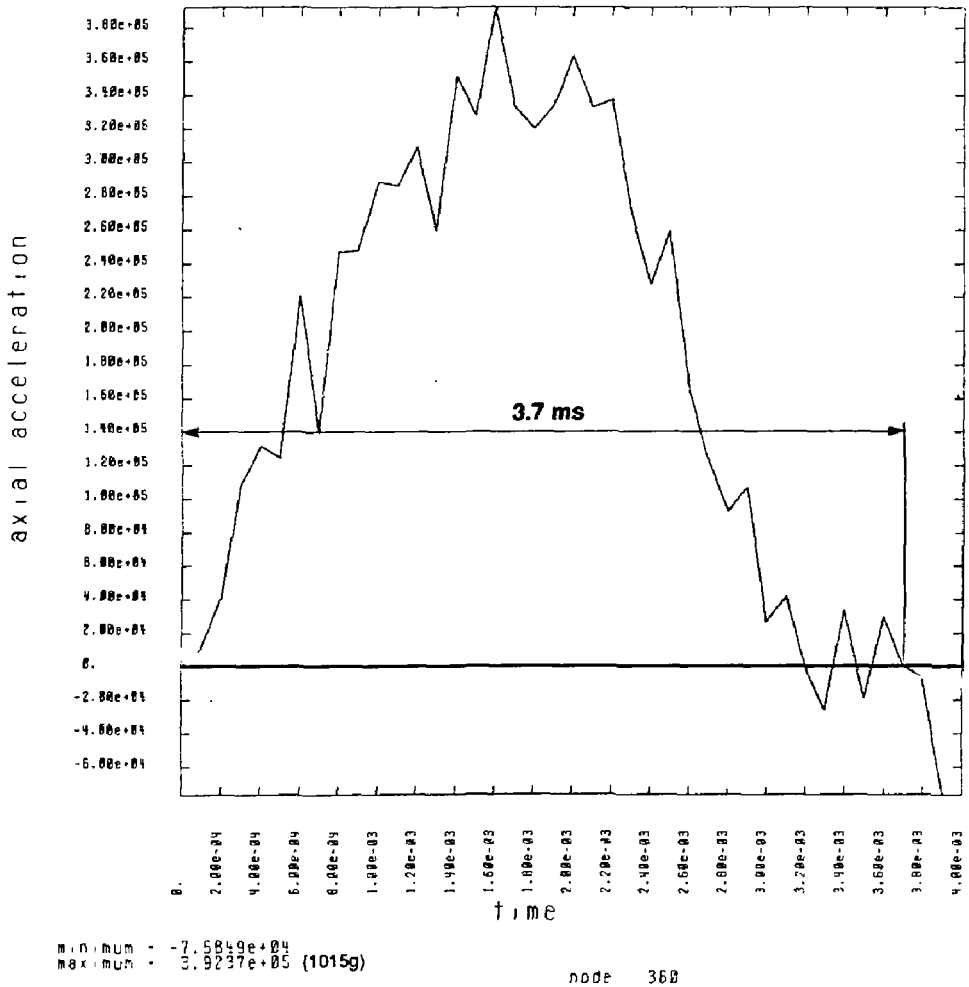

Figure 3-18 Computed deceleration time history for 30 foot round end drop.

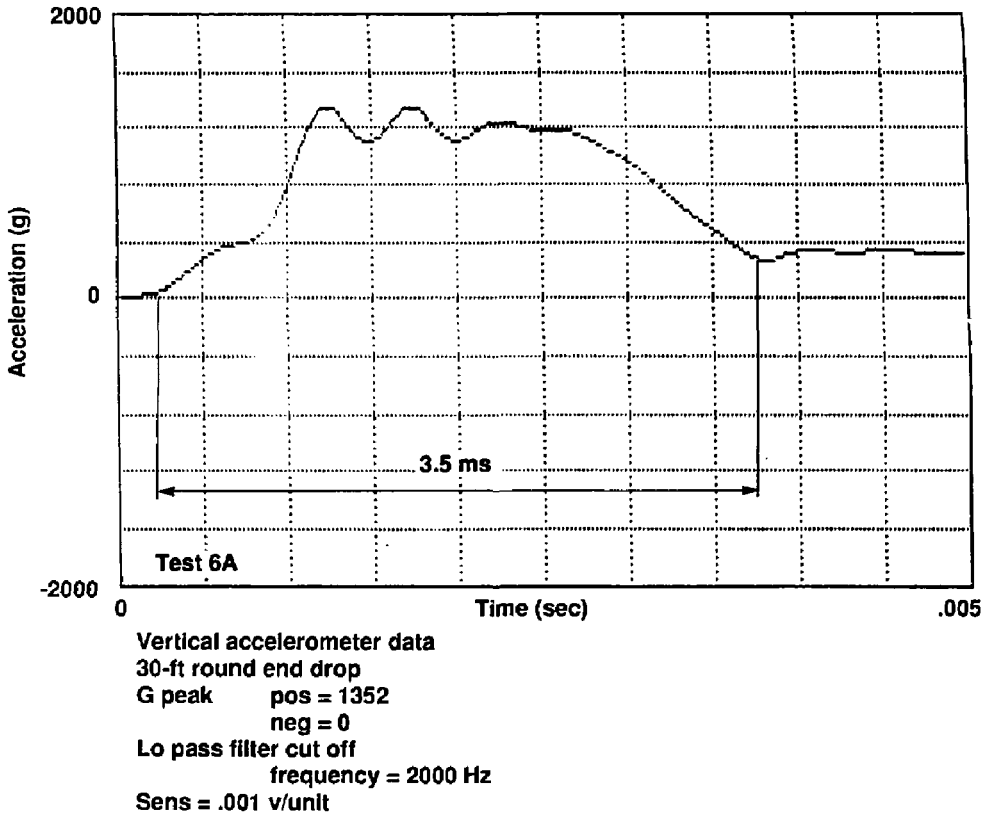

Figure 3-19 Experimental deceleration time history for 30 foot round end drop.

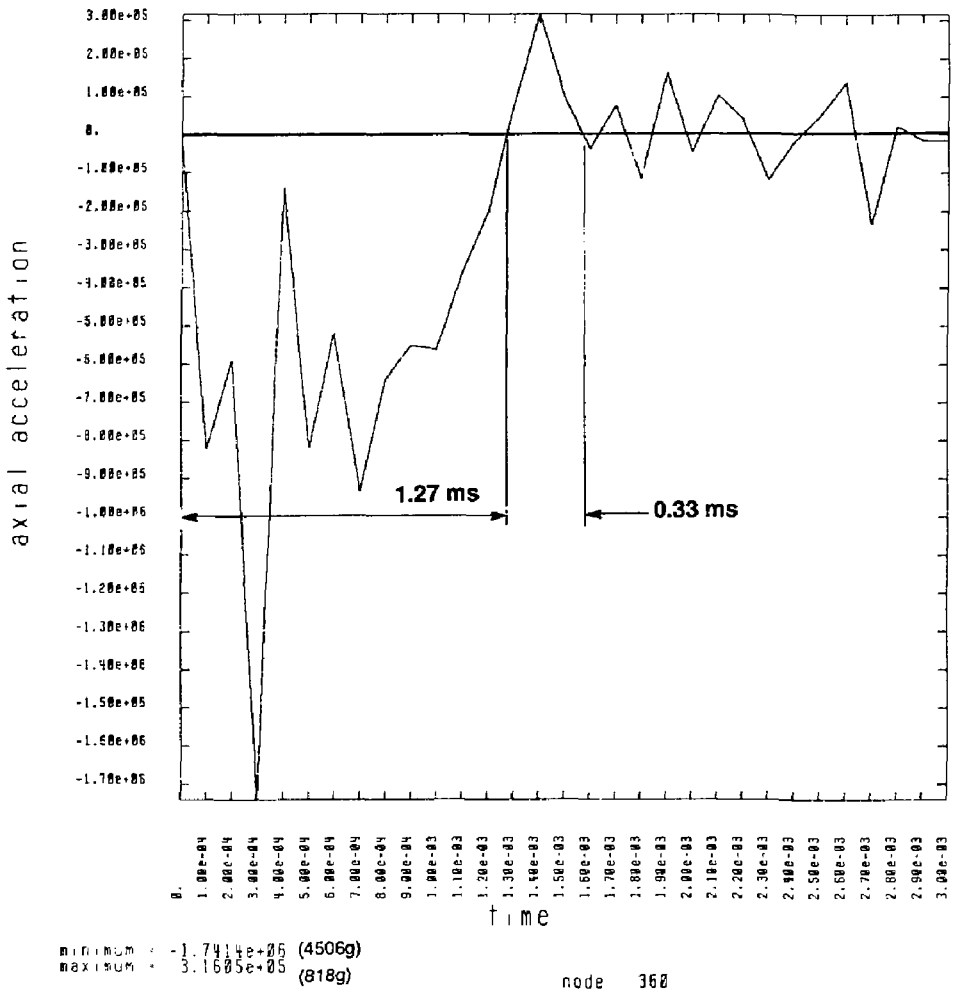

Figure 3-20 Computed deceleration time history for 30 foot flat end drop.

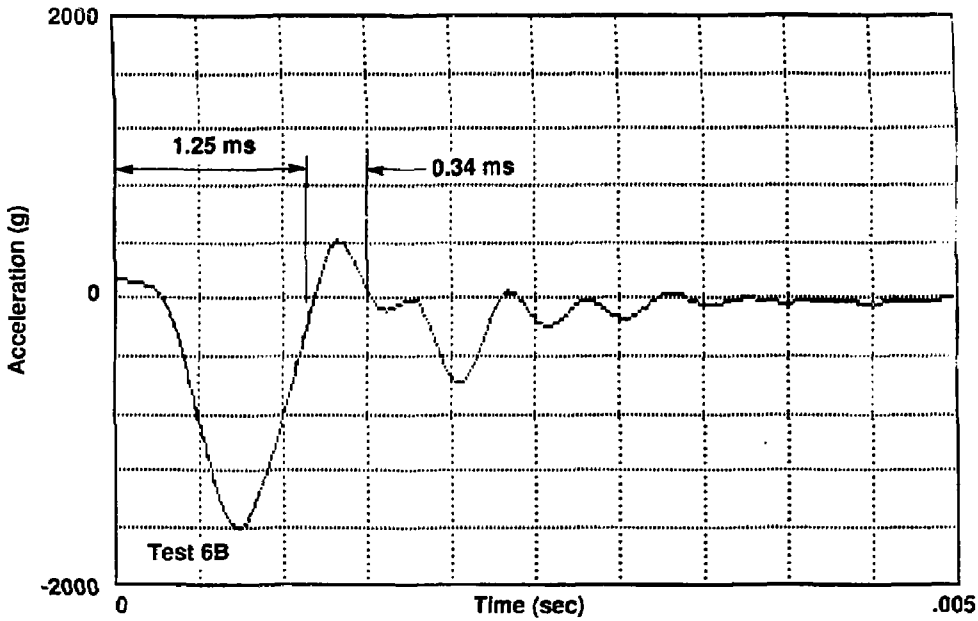

Figure 3-21 Experimental deceleration time history for 30 foot flat end drop.

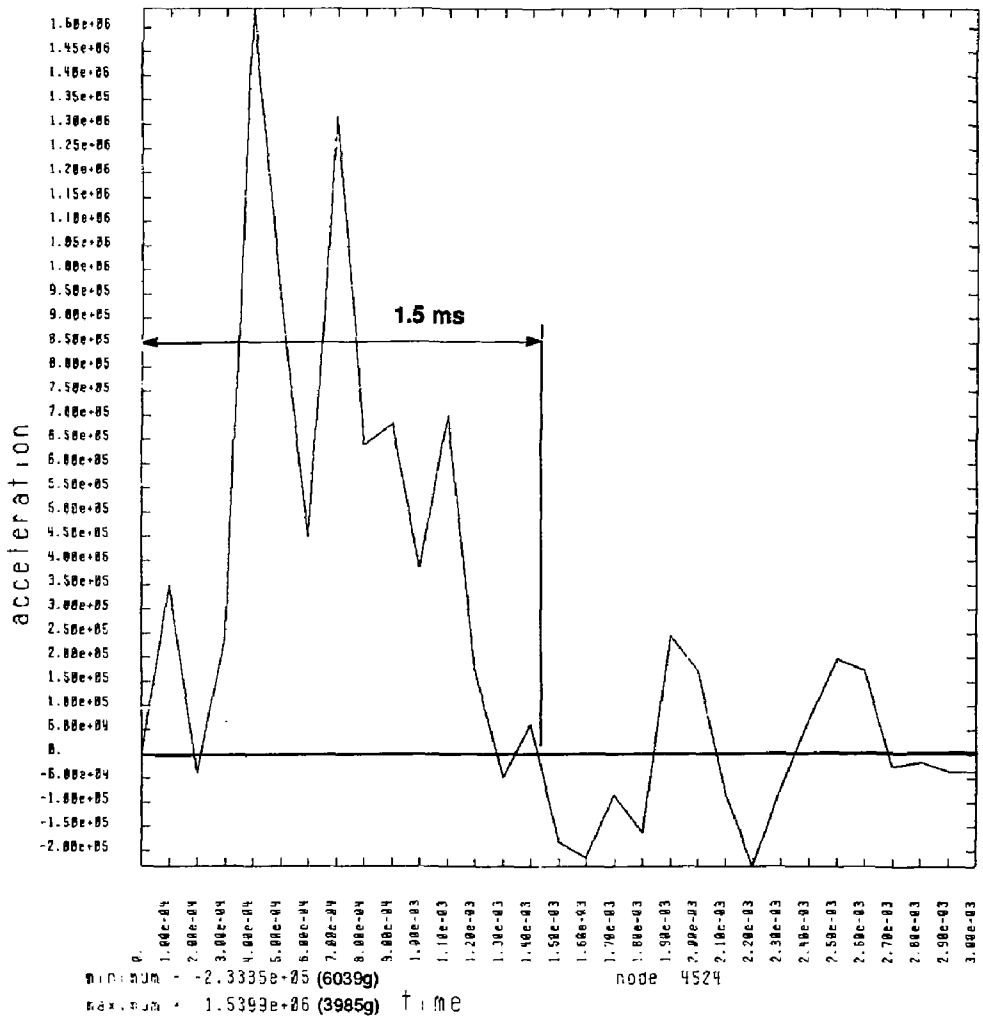

Figure 3-22 Computed deceleration time history for 30 foot side drop.

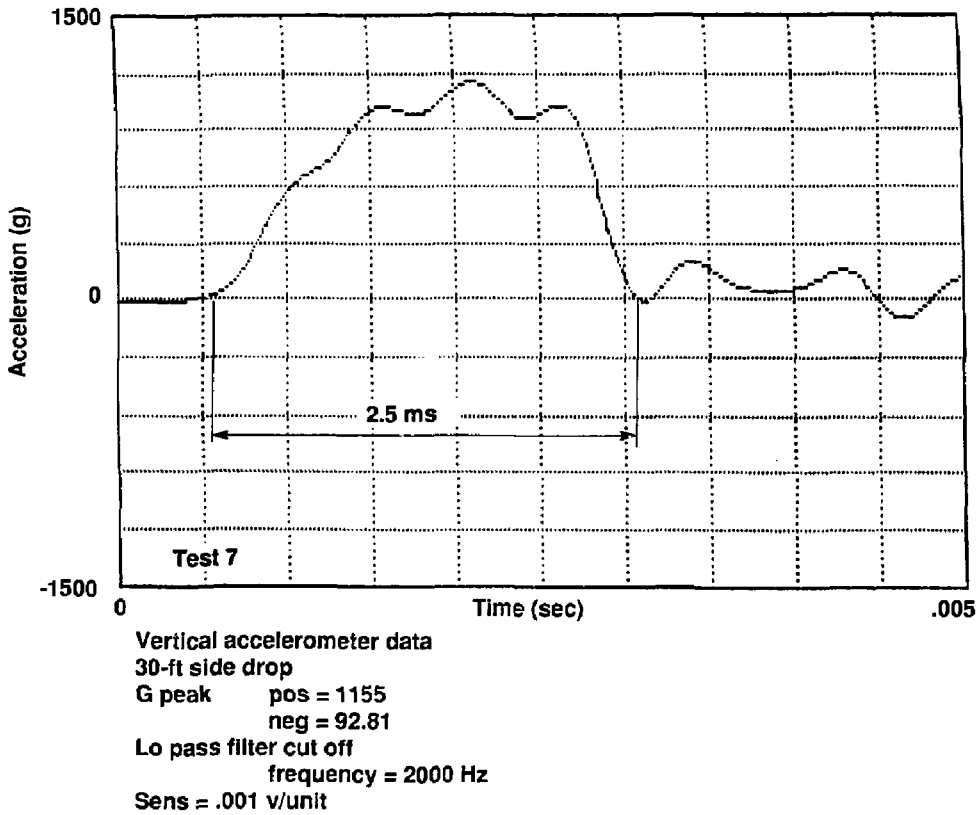

Figure 3-23 Experimental deceleration time history for 30 foot side drop.

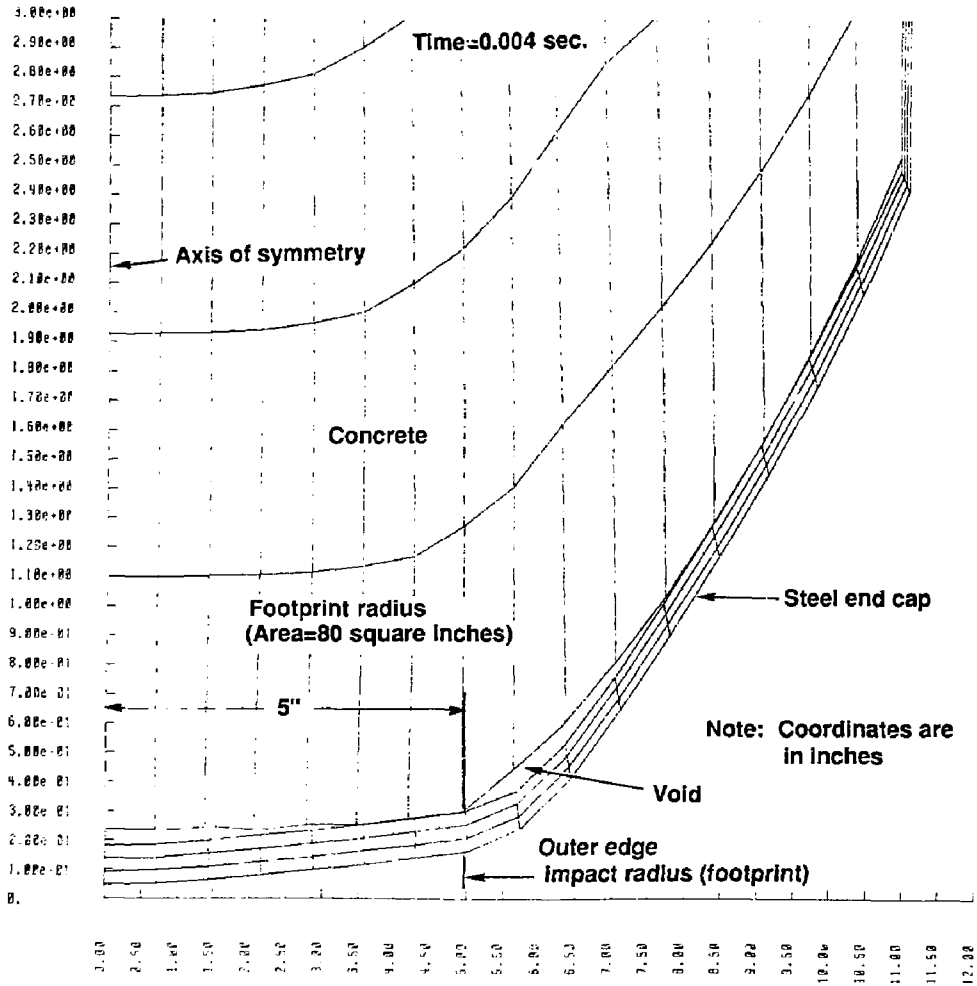

Figure 3-24 Analytically predicted deformation due to 30 foot round end drop. (Footprints, the flattened impact area, from the experimental drops are shown in Figures 3-25 and 3-26.)

Figure 3-25 Footprint from 30 foot round end drop (Specimen 1A). (The squares on the specimen are 0.5 inches on a side. The background squares of 1 foot are for analysis of the drop, Courtesy WHC.)

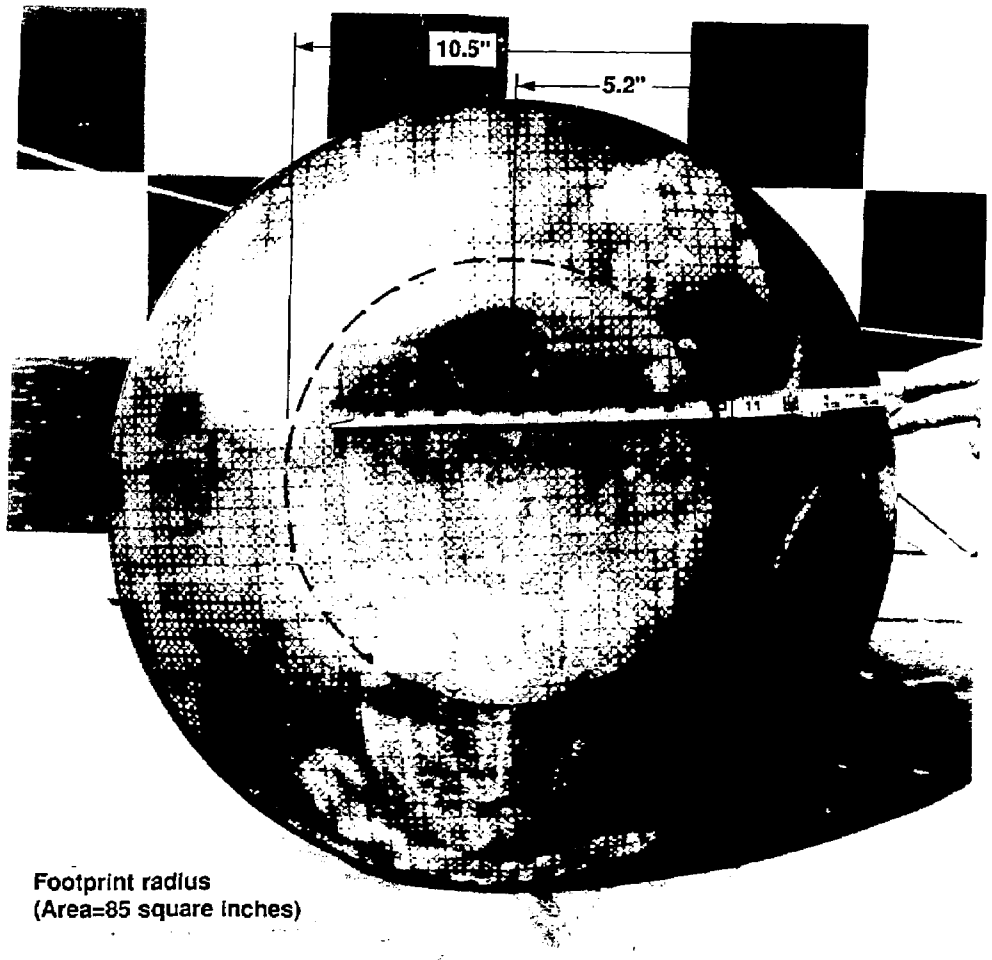

Figure 3-26 Footprint from 30 foot round end drop (Specimen 6A). (The squares on the specimen are 0.5 inches on a side. The background squares of 1 foot are for analysis of the drop, Courtesy WHC.)

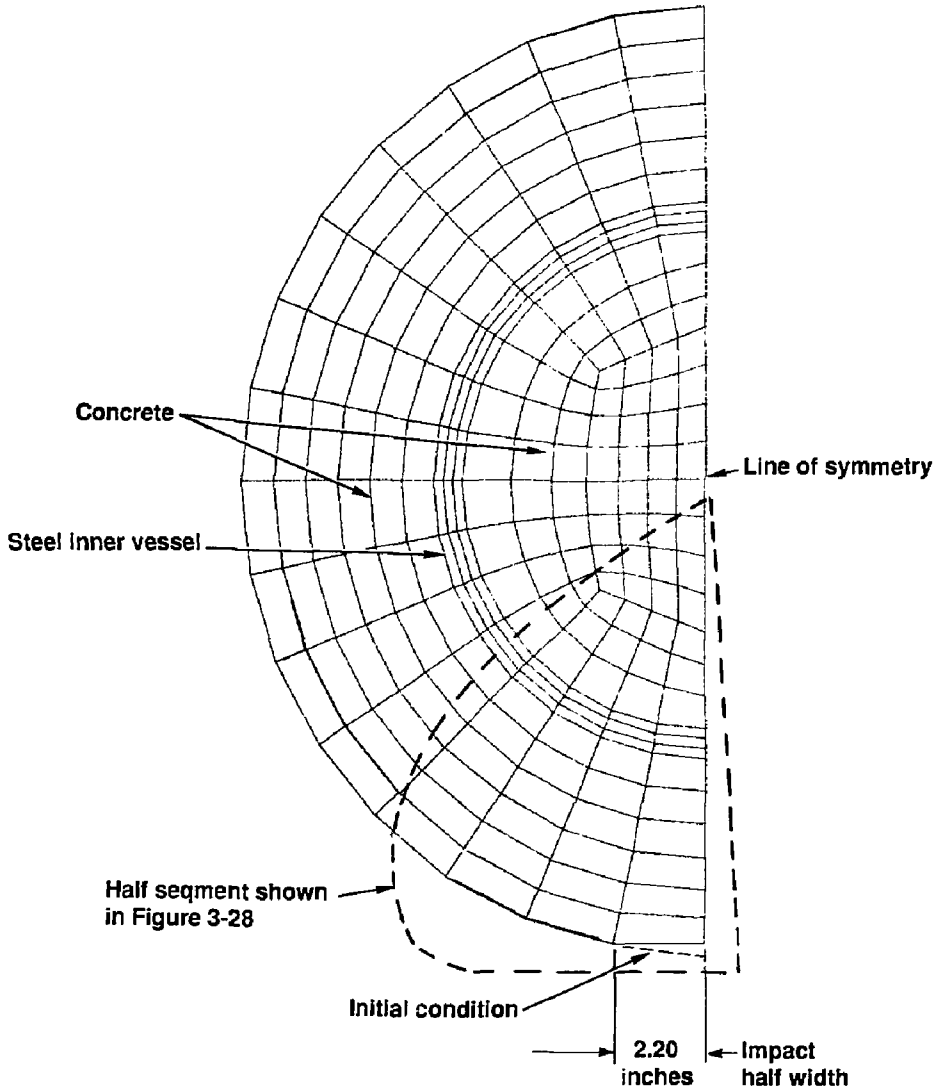

Figure 3-27 Analytically predicted deformation due to 30 foot side drop. (The footprint area is 210 square inches. Compare to experimental result shown in Figure 3-28.)

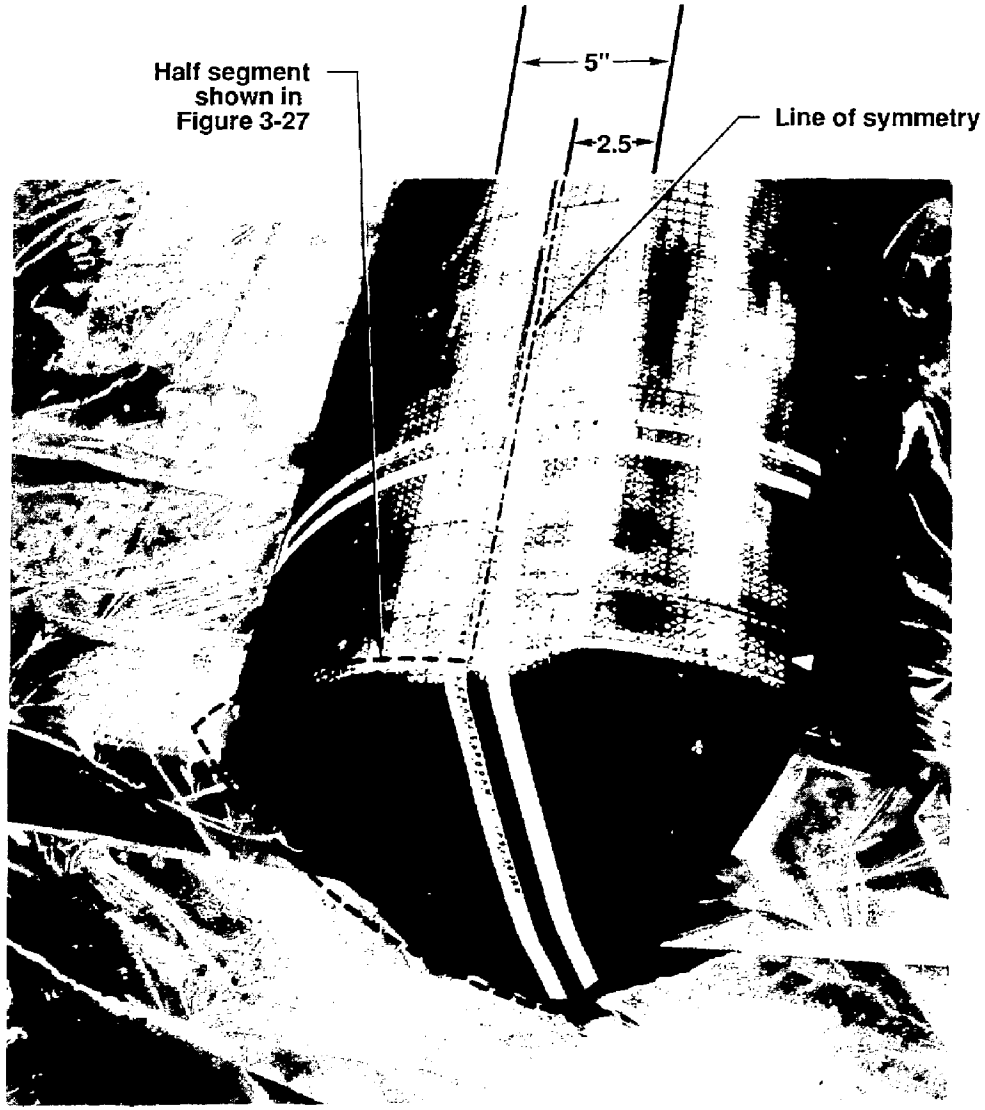

Figure 3-28 Partial footprint from 30 foot side drop (Specimen 2B). (The squares on the specimen are 0.5 inches on a side. The footprint area is 270 square inches, Courtesy WHC.)

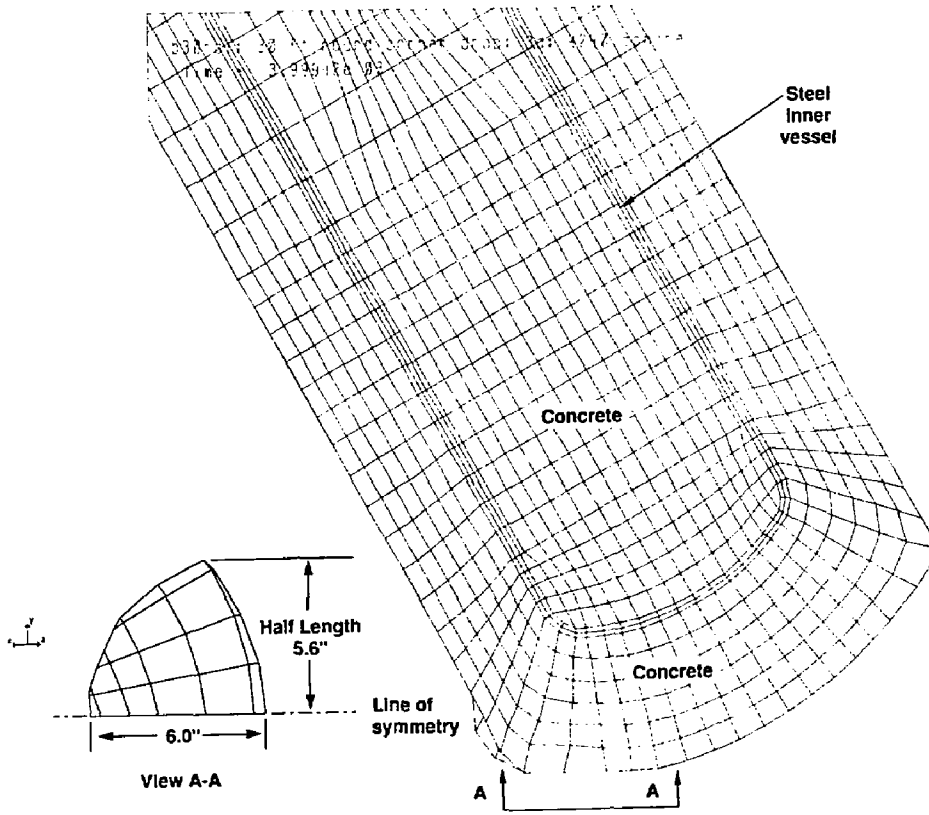

Figure 3-29 Analytically predicted deformation due to 30 foot round end corner drop. (Compare to experimental results shown in Figure 3-30.)

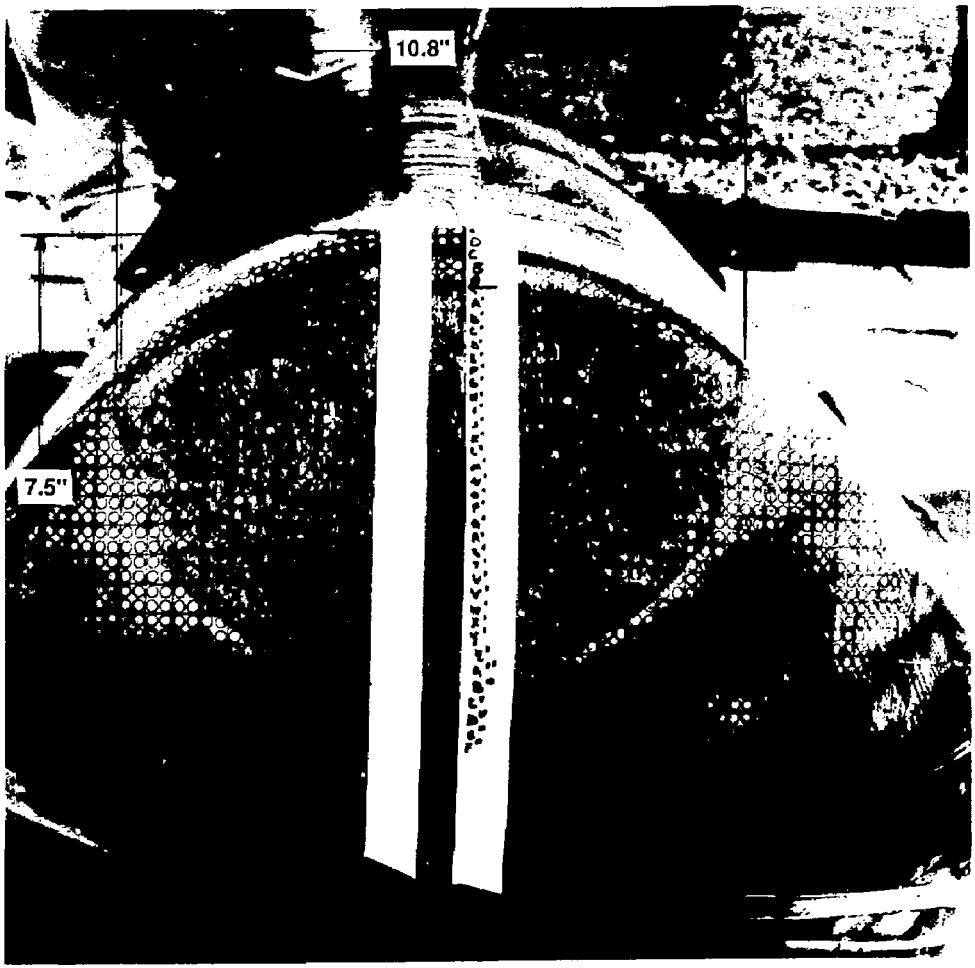

Figure 3-30 Footprint from 30 foot round end corner drop (Specimen 3A). (The squares on the specimen are 0.5 inches on a side. Courtesy WHC.)

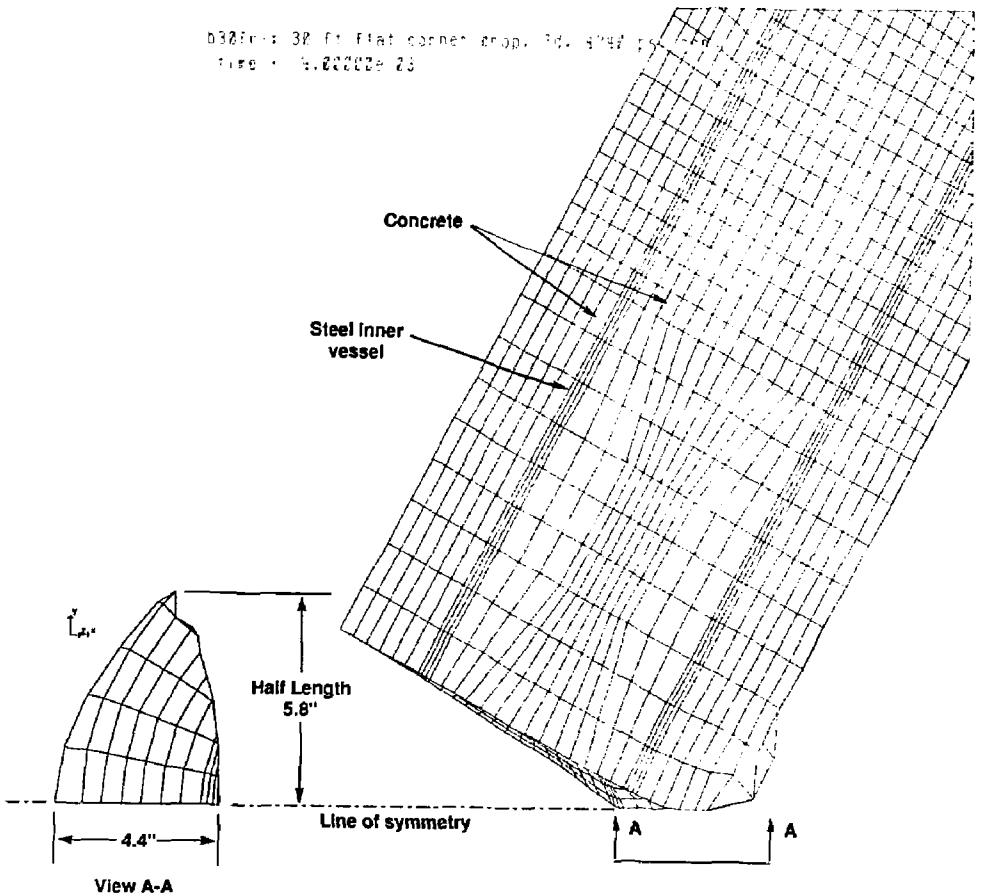

Figure 3-31 Analytically predicted deformation due to 30 foot flat end corner drop. (Compare to experimental results shown in Figure 3-32.)

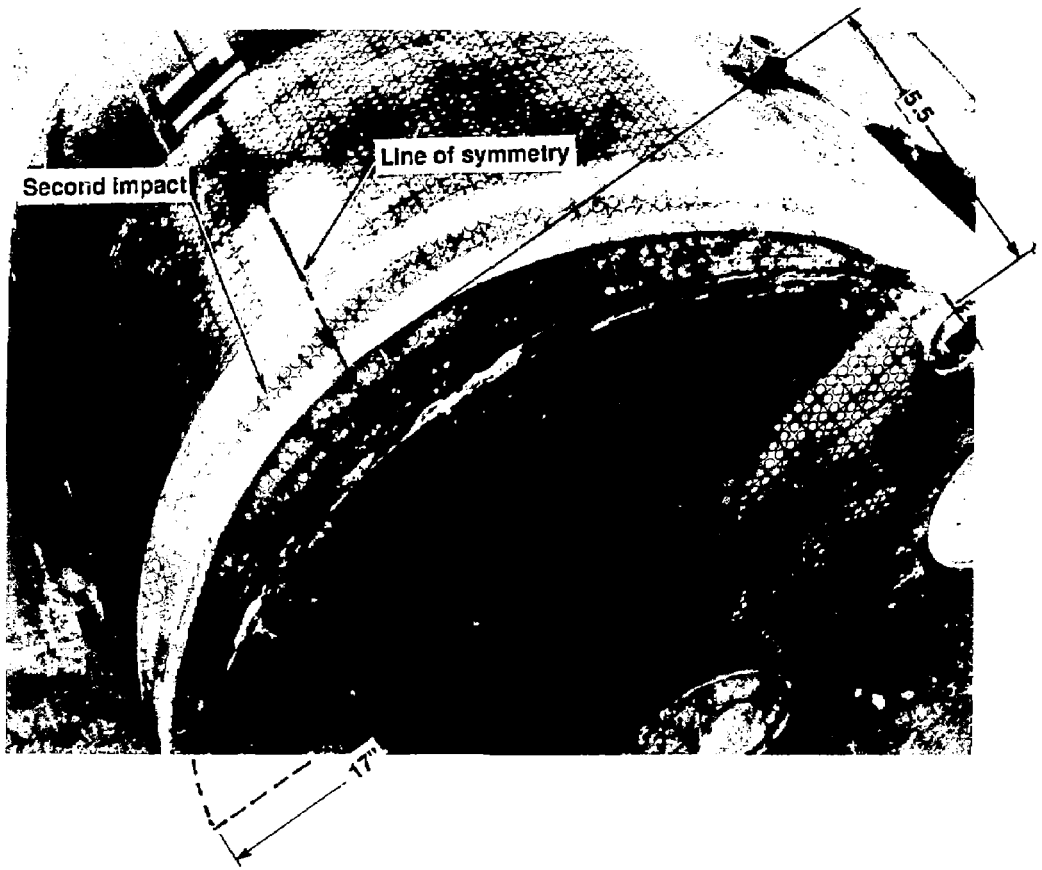

Figure 3-32 View of impact area from 30 foot flat end corner drop (Specimen 3B). (The squares on the specimen are 0.5 inches on a side. Courtesy WHC.)

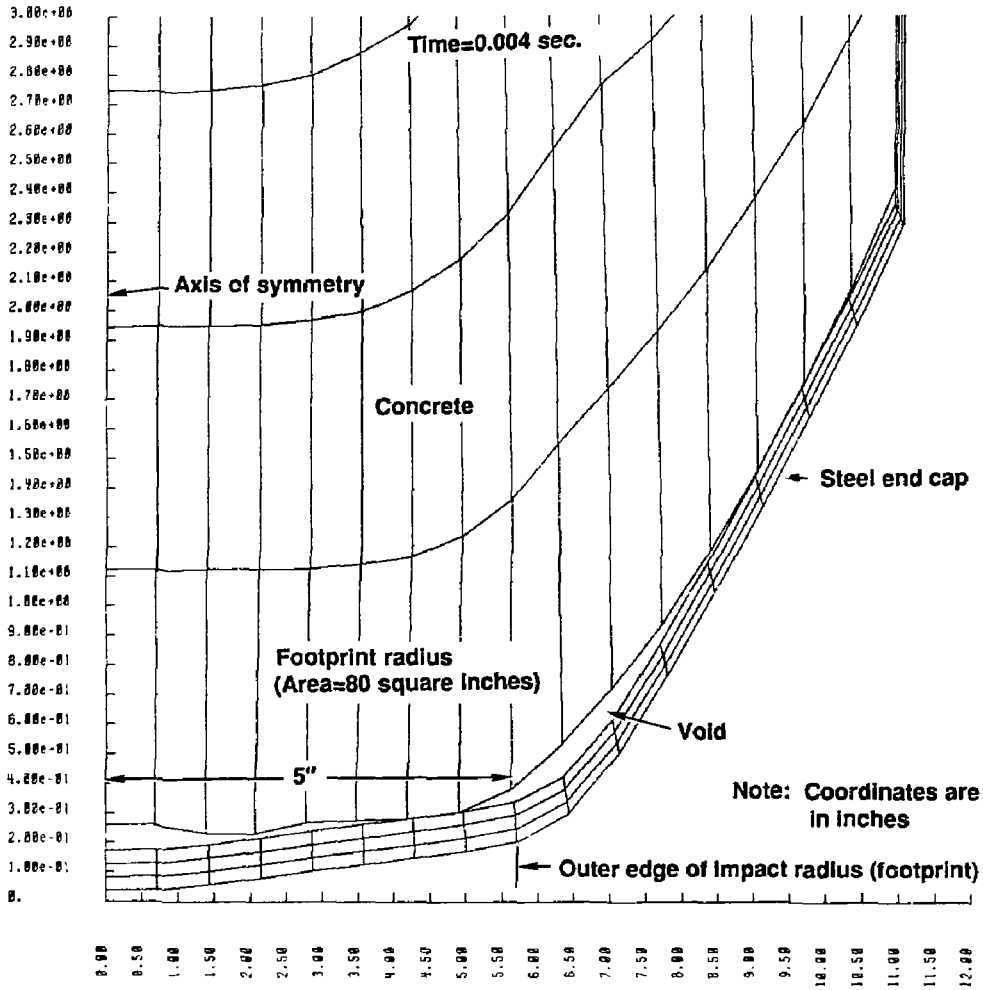

Figure 3-33 Analytically predicted deformation due to 45 foot round end drop. (Compare to experimental results shown in Figure 3-34.)

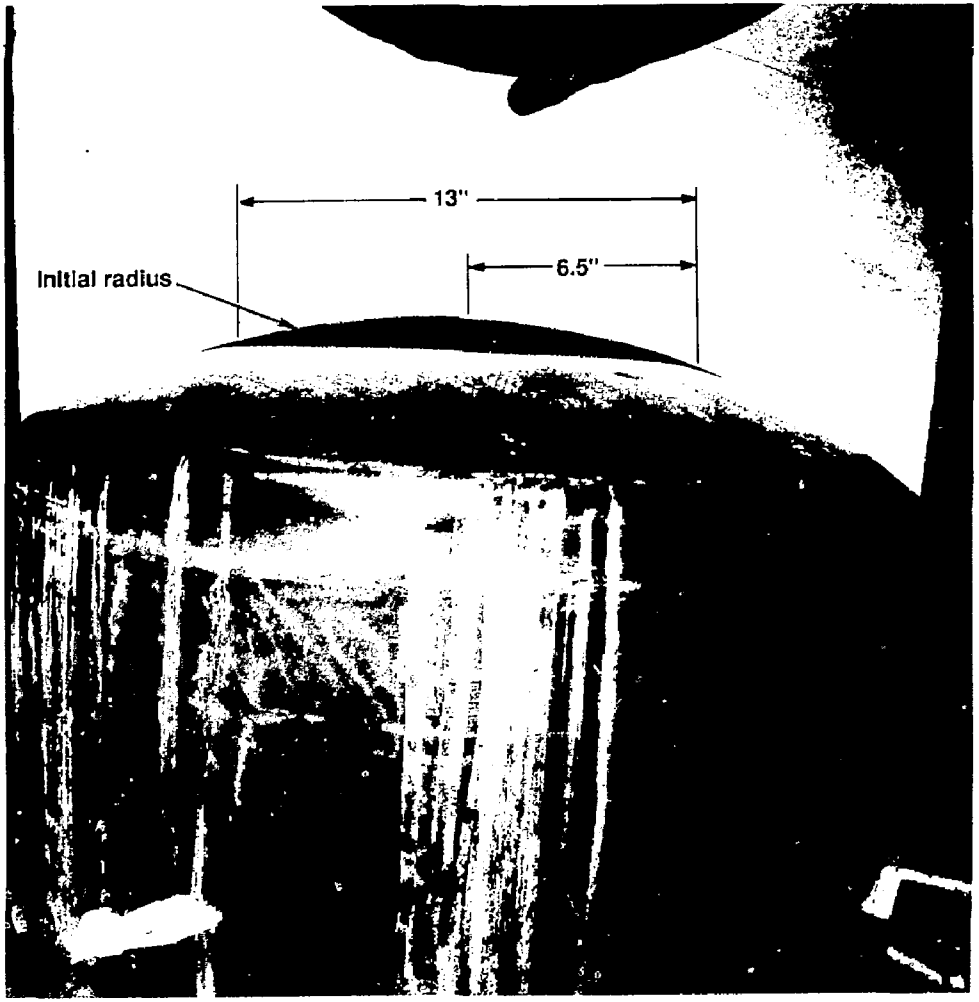

Figure 3-34 Side view of impact area from 45 foot round end drop (Specimen 4). (Footprint area is 130 square inches, courtesy WHC.)

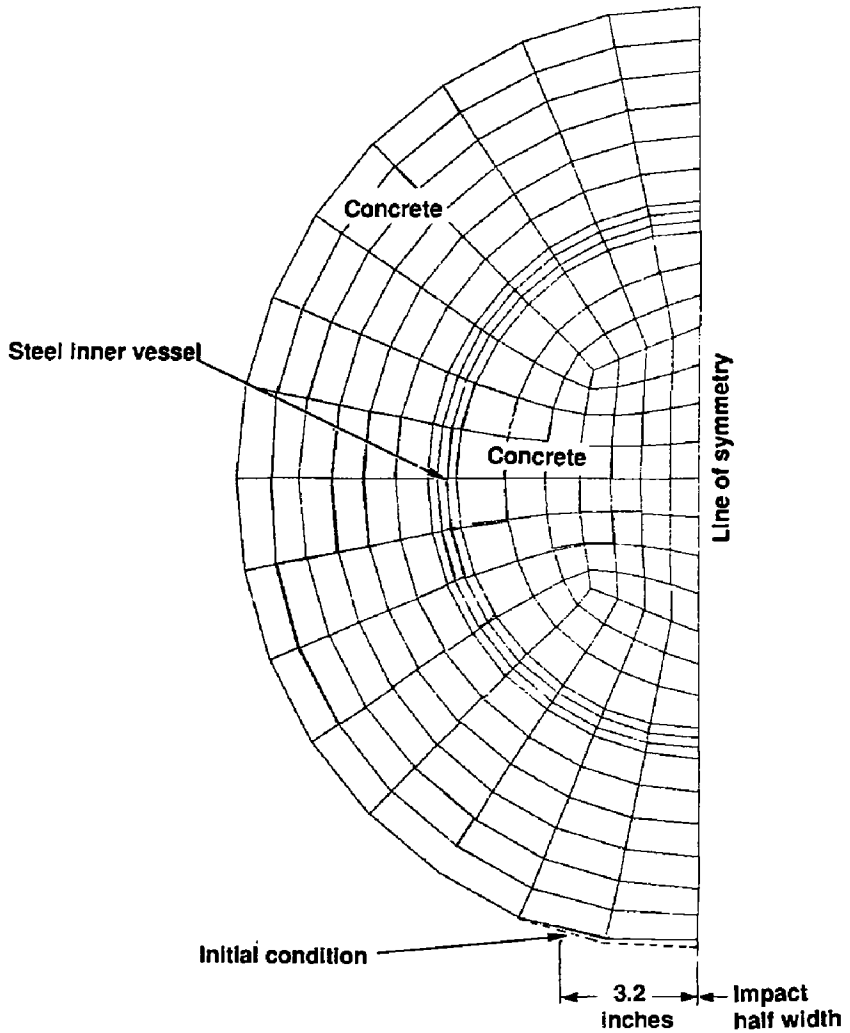

Figure 3-35 Analytically predicted deformation due to 45 foot side drop. (Compare to experimental results shown in Figure 3-36.)

Figure 3-36 View of impact area from a 45 foot side drop (Specimen 5). (The footprint area is 310 square inches. Courtesy WHC.)

4.0 Structural Evaluation for Impact Loads

4.1 Introduction

This section of the report addresses the structural evaluation of the package under impact loads. The acceptance criteria adopted as a basis for design as stated in Section 1.3, require the outer shell to confine the concrete and RPV with the radioactive components under normal and accident conditions. This means that while plastic deformation and local rupture may be possible under various accident scenarios, such plastic deformation and local rupture should not prevent the outer shell from providing effective confinement. The position adopted in this structural evaluation is that gross plastic deformation by itself will not significantly reduce confinement and shielding capability. Only large distortion that progresses far enough to cause gross rupture is of significance. Consequently, the results of the structural analysis of the outer shell are compared with a strain limit state to assess the margin of safety against rupture. The limit state selected and its application to the outer shell are discussed in subsection 4.2-4.3.

In addition, the acceptance criteria also requires the RPV wall and the NST concrete to provide shielding under normal and accident conditions. Since the concrete will fracture on impact, it is desirable that the RPV wall not become crazed upon impact with through cracks which could allow radiation streaming from the internal radioactive components. The position adopted in the evaluation is that, assuring ductile behavior, cracking of the RPV wall will not occur when the membrane stress in the wall is below the yield point for the steel material. Consequently, the stress in the RPV wall should be less than 72 ksi to assure that no cracking occurs.

4.2 Limit State to Prevent Rupture

For both the normal condition (1-foot drop) and the hypothetical accident condition (30-ft drop), the analysis shows that the outer shell confinement barrier is strained well beyond yield at points of impact. Since this outer shell contributes toward maintaining the integrity of the concrete shielding

and preventing dispersion of the radioactive components, it is desirable that it not rupture even though it may undergo considerable plastic deformation. This condition can be satisfied, provided the strains are less than the strain at rupture revealed by a tensile test. Unfortunately, the elastic/plastic finite element analysis using plate elements does not provide valid strain data when the strain exceeds the amount associated with plastic instability or the onset of necking of the material. Furthermore, beyond necking instability, the strain at rupture is not well characterized for biaxial stress states. Thus one cannot reliably determine a margin of safety against the strains at rupture. The limit of validity of the computed strain levels is the strain at the onset of necking instability, which is adopted as the limit state criterion. The onset of necking instability for uniaxial loading is defined by the condition

$$\sigma = d\sigma/d\bar{\varepsilon} , \tag{4-1}$$

where σ and $\bar{\varepsilon}$ are the coordinates of points on the true stress - true strain curve for the material (Ref. 10). The strain associated with this stress is the strain limit state criterion, ε_u which is the strain corresponding to the engineering tensile strength. This limit state is adopted because, for a ductile material, it is the threshold above which rupture is possible and below which it is not.

4.3 Restrictions on Use of a Strain Criterion

Before presenting an evaluation of the structural integrity of the Shippingport package, it is important to define the restrictions under which the use of a plastic strain limit is applicable To put the matter in some perspective we should be aware that for Category I primary containments, stresses must be within the elastic limit for normal conditions, which includes the 1-ft drop. For accident conditions (30-ft drop) the allowable stresses, calculated elastically, are such that a small amount of plastic deformation is tolerated. At this time strain limits have not been defined for Category I primary containments. For lower radioactive contents

represented by Category II or III containments no structural analysis criteria have been defined and a case may be made for a failure criterion based upon strain, provided that an adequate margin of safety is provided against rupture.

The restrictions alluded to, within which a strain criterion may be applicable, will now be discussed. In the first place, the criterion is only valid for impact-type loadings of relatively short duration and limited energy content. It does not apply to steady-state loads such as constant pressure or dead weight wherein the inception of yielding is tantamount to progressive gross deformation and rupture. Equally important is the requirement that the material have sufficient toughness to preclude brittle fracture at stresses below yield at the lowest service temperature. Nor should the material contain flaws or cracks so large that ductile tearing instability is initiated in the plastic regime.

4.4 Limit States for Confinement Boundary

The limit state defined by Eq. 4-1 is only applicable to a uniaxial state of stress. For the biaxial condition it is expressed by

$$\alpha\sigma = \frac{d\sigma}{d\varepsilon} , \qquad 4\text{-}2$$

where α is determined by the degree of biaxiality. Analyses based upon uniform biaxial strain prior to necking instability leeds to the following expression,

$$\alpha = 1 + \rho , \qquad 4\text{-}3$$

where ρ is the ratio of the minimum principal stress to the maximum principal stress. For uniaxial stress $\rho = 0$ or $\alpha = 1$. For equibiaxial stress, $\rho = 1$ and $\alpha = 2$. Equation 4-3 provides values of α for intermediate values of ρ.

Assuming that stress strain behavior in the plastic region is governed by

(Ref. 9)

$$\sigma = C\varepsilon^n \qquad 4\text{-}4$$

it can be shown that

$$\frac{d\sigma/d\varepsilon}{\sigma} = \frac{\varepsilon_u}{\varepsilon} , \qquad 4\text{-}5$$

where ε_u is the true strain corresponding to the engineering tensile strength. Consequently, the limit state strain for any condition of biaxiality is

$$\varepsilon_\alpha = \frac{\varepsilon_u}{\alpha} = \frac{\varepsilon_u}{1+\rho} . \qquad 4\text{-}6$$

Strain limits as a function of the ratio of the principal stresses are shown in Figure 4-1 for SA-212 B and A-36 steels.

It should be noted that there is still a margin between the strain at necking instability and the strain at ductile rupture. However, for reasons previously explained, this margin is not easily assessed and is not invoked except to point out that there is greater margin against ductile rupture then indicated by the margin against necking instability.

4.5 Description of Analysis Methods

Department of Energy regulations require that Type B shipping containers meet the requirements of 10 CFR 71. These requirements include a series of impact tests for normal and hypothetical accident conditions of transport.

The normal impact test required for the shipping package is a free drop of one foot onto a flat, unyielding horizontal surface, striking the surface in a position for which maximum damage is expected. The hypothetical accident impact test required is a free drop from thirty feet onto a flat, unyielding horizontal surface, again striking the surface in the orientation expected to produce the greatest damage.

In order to meet these regulations, a series of dynamic finite element analyses were performed with DYNA3D--a three-dimensional, nonlinear, dynamic analysis code. The results of these analyses are described in Section 4.7. Material properties used in the finite element material models are described in Section 2.2.

In order to show that analyses using DYNA3D can properly describe actual behavior during impact conditions, a benchmark study combining tests and DYNA analyses was conducted. This study is described in Chapter 3.0.

4.6 Finite Element Analysis Models

The three-dimensional finite element model was generated using the finite element mesh generator SLIC [Ref. 7]. This full size complete model of the Shippingport package was used to perform detailed impact analyses of the package. The Shippingport package model is composed of concrete surrounding the vessel, grout inside the vessel, the head and flange, the vessel itself including the nozzles, insulation surrounding the vessel, the ring girder, the outer shell, the plates making up the lifting beam, and bolts attaching the lifting beam to the head. The 16 lifting bolts between the lifting beam and RPV closure head are modeled as 16 circular beams. The 42 bolts between the closure head and vessel flange are modeled as 16 bolts with increased cross sectional areas. The shell/concrete and lifting beam/concrete interfaces are modeled as frictionless contact surfaces which disallows normal forces between the shells and the concrete. An exploded view of the model is shown in Figure 4-2. This full size model was used for the detailed impact analysis of the package. Table 4-1 summarizes the characteristics of the finite element model.

4.7 Analysis Results

A summary of the strain results of the impact analysis for the outer shell, which consists of the NST, the skirt and the lower end plate of the lifting beam is shown in Table 4-2. The last column provides the margin of safety against reaching the strain limit state. A summary of the stress

results of the impact analysis for the RPV is shown in Table 4-3. The stresses in the RPV are generally low except in the vessel/nozzle junction region. The stresses in this region are not high for the 30-ft corner drop on the flat end due to the fact that the nozzle is far away from the impact zone.

The details of the impact analyses are discussed in the following subsections, however, the orientations of most interest are the 30 foot drop on the side and the 30 foot drop on the flat end corner. The 30 foot side drop is critical because localized cracking might occur in the end plate and outer shell, whereas, the 30 foot flat corner drop is critical because the bolts holding the vessel closure in place are subjected to high shear forces.

4.7.1 1-Foot Side Drop

This analysis was performed with DYNA3D, using the half-symmetry model of the full Shippingport package. The analysis uses an initial velocity of 96.3 in/sec in the negative y direction of the model. Maximum principal strains in the shell and end plates do not exceed the limit state strain criterion. In addition, stresses in the RPV do not exceed the elastic limit for the material.

4.7.2 30-Foot Side Drop

This analysis was performed with DYNA3D, using the half-symmetry model of the full Shippingport package. The analysis uses an initial velocity of 527.5 in/sec in the negative y direction of the model. Maximum principal strains in the NST are below the limit state strain. In both the skirt and the lower end plate the strains exceed the limit state value. In fact, the 0.676 strain in the end plate is sufficiently high that it is reasonable to expect ductile rupture to occur. However, as shown in Figure 4-3, which displays the maximum principal stress contours, this principal strain is highly localized and though rupture may initiate at the point indicated on the figure, this rupture will arrest before reaching the values corresponding to contour B, namely 27.8 ksi, which is in the elastic strain region. In the skirt, a maximum principal strain of 0.174 does exceed the 0.129 limit state strain for A-36. However,

ductile rupture may not be initiated since the strain pattern is nearly uniaxial and the maximum principal strain is less than the uniaxial fracture strain of 0.20. In any event, as shown in Figure 4-4 which displays the maximum principal stress contours, the principal strain is highly localized. Should rupture initiate at the point indicated on the figure, this rupture will arrest before it reaches contour E, namely 32.3 ksi, which is in the elastic region.

Figure 4-5 shows the contours of maximum principal stress in the vessel/nozzle junction region. It is clear that, while the stresses are high in this junction region, these stresses drop off rapidly away from this region. since the radiation source is mainly in the middle of the RPV and is far away from this nozzle region, radiation streaming is expected to be low if a crack develops in this localized region.

4.7.3 30-foot Flat End Drop

This analysis was performed with the DYNA3D code using a quarter symmetry model to represent the complete Shippingport package. The analysis assumes an initial velocity of 527.5 in/sec corresponding to a 30-ft drop, in the negative x direction of the model. Maximum principal strains in the skirt and lower end plate do not exceed the limit state strains, with a large margin.

4.7.4 30-foot Round End Drop

This analysis was performed with DYNA3D, using the quarter-symmetry model of the full Shippingport package. The analysis uses an initial velocity of 527.5 in/sec in the positive direction of the model. Maximum principal strains in the NST domed end do not exceed the limit state strains.

4.7.5 30-foot Corner Drops

According to 10 CFR 71, the package is subjected to a 30-ft free drop onto a flat, essentially unyielding, horizontal surface, striking the surface in a position for which maximum damage is expected. In the finite element analysis of the Shippingport package, a worst impact angle needs to be

determined before a corner drop analysis can begin; otherwise, many analyses with various impact angles would have to be performed to capture the worst package orientation. Performing many corner drop analyses is not practical because the complete Shippingport finite element analysis model used here is quite large, and computation cost is high.

To select the worst impact angle, we used the three-dimensional benchmark model (Figure 3-3) and a simplified Shippingport model. This model, although much simplified compared to the complete Shippingport package model, still retains the overall characteristics of the package. By comparing the analysis results for many drop angles and studying the stress and strain conditions of these models, a reasonable selection can be made.

The benchmark model was used to perform a series of analyses to determine the worst package orientation for the corner drop on the rounded end. Table 4-4 shows the stress and strain results for impact angles of 15, 30, and 62 degrees from horizontal. The case with 62 degrees corresponds to the CG-over-corner impact orientation. The CG-over-corner case clearly dominates other cases and is expected to produce the greatest damage for both the NST and RPV.

For the flat end corner drop, Table 4-5 shows the stress and strain results for impact angles of 5, 30, and 62 degrees from horizontal. The 62-degree case corresponds to the CG-over-corner impact orientation. It is apparent from the variation of effective plastic strain with drop angle for the outer shell that the worst damage will be experienced for very shallow angles. As a limit, the worst orientation for the outer shell is the side drop, which was already considered in Paragraph 4.7.2. For the RPV, the worst orientation still appears to be the CG-over-corner impact orientation.

For both the flat end and round end corner drops none of the primary principal strains in the skirt or the NST exceeds the strain limit state. Of greater concern for the flat end corner drop is the effect of a lateral shear force on the bolts attaching the RPV head to the vessel. To determine the critical drop angle for the maximum shear force in the plane of the RPV flange, we computed acceleration as a function of drop angle as shown in Table 4-6. It appears that the deceleration increases as the drop angle

decreases. However, the reaction force from the unyielding surface causes the contact area in the outer shell to extend beyond the lower end plate of the lifting beam as the drop angle decreases (Fig. 4-6). As a result, the reaction force in the outer shell region reduces the total shear on the plane of the RPV flange. We regard drop angles between 15 and 20 degrees to be most critical since the contact area extends only slightly beyond the end plate. Therefore, the analysis for the corner end drop was performed with drop angles of 15 and 20 degrees.

Even though the closure studs are seated in spherical washers, they were conservatively modeled as beam elements fixed at both ends. The shear forces on the studs cause bending stresses to exceed the yield strength at the assumed built-in ends. Consequently, the rotations at the built-in ends allow lateral displacement of one end of the stud relative to the other. Since the distance between the flanges is fixed, this lateral displacement tends to stretch the stud thereby inducing axial stresses. A survey of the elements representing the studs show that the maximum axial and shear stresses vary respectively, between 3.2 to 10.0 ksi and 34 to 55 ksi. The yield strengths of the stud material are 100 ksi in tension and 60 ksi in shear. Consequently, even though the bending stresses at the built-in ends exceed the yield strength, the studs maintain their structural integrity. It is clear that the outer shell is taking most of the load during impact.

4.8 Sensitivity of Concrete Strength

A sensitivity study was performed to evaluate the effects of concrete compressive strength on the Shippingport package. This study was performed prior to the development of structural evaluation criteria. The parameters selected for this study are the maximum effective plastic strain for the outer shell and the maximum effective stress for the RPV. These parameters are good gauges for measuring material distortion.

Figure 4-7 shows the variation of these parameters as a function of concrete compressive strength. They are normalized with respect to their values at 2000 psi concrete compressive strength. It is clear that the

material distortions in the RPV and the outer shell are not very sensitive to the variations in the concrete compressive strength. There is a maximum of 15% variation in these parameters for 100% increase in concrete compressive strength from 2000 to 4000 psi. It is expected that the results present in this report will not be severely affected if the actual date of package transport varies from the current estimate of eleven months after initial concrete fill.

4.9 Summary and Conclusions

The purpose of this analysis was to evaluate the structural response of the Shippingport package to the normal and accident conditions defined by 10 CFR 71. The acceptance criterion for the structural response was determined by the technical basis for design described in paragraph 1.3. The acceptance criterion takes the form of a strain limit state defined by the onset of necking instability. The structural analyses show that there is only one condition, namely the 30 ft side drop, in which the maximum principal strains exceed the limit state criterion to the extent that the likelihood of local ductile rupture is high at the juncture of the skirt and lower end plate. Because of the large stress gradient, the rupture will not progress far enough to compromise the ability of the outer shell to perform its function of protecting the concrete shielding and confining the radioactive components as long as brittle fracture is of no concern. The reactor pressure vessel experiences stress levels in the vicinity of the nozzle wall/vessel junctions that exceed yield. Since the brittle fracture properties of the RPV are not known, it has to be assumed that local cracking will occur at the peak of the stress gradients at the nozzle junctions. However, since the RPV is not relied upon as the primary confinement barrier, the worst consequence of the formation of cracks is the possibility of radiation streaming from the interior of the RPV. As long as the concrete shield remains intact, the radiation from the cracked RPV will have little effect upon the environment and will not exceed regulatory limits.

Table 4-1 Complete Shippingport Package Model

Number of Nodes:	26795
Number of Brick Elements:	18096
Number of Shell Elements:	3074
Number of Thick Shell Elements:	3440
Number of Beam Elements:	40

Component	Elements/Class	Material Model
Concrete Outside PPV	7320 Bricks	Pseudo TENSOR Geological
Grout Inside RPV	7560 Bricks	Elastic
Head and Flange ASTM A508(-67) Class 4	1928 Bricks	Elastic-Plastic
RPV Nozzles ASTM SA302 Grade B	3152 Thick Shells	Elastic-Plastic
Insulation Fiber Insulation	1288 Bricks	Crushable
Ring Girder (NST) ASTM SA201 Grade B	288 Thick Shells	Elastic-Plastic
Outer Shell ASME SA212 Grade B - NST ASME SA36	1432 Shells	Elastic-Plastic
Lifting Beam ASME SA36	1642 Shells	Elastic-Plastic
Lifting Bolts ASME SA36	40 Beams	Elastic-Plastic

Table 4-2 Summary of impact analysis results for outer shell.

Impact Orientation	Structure	Material	Maximum Principal Strain	Maximum Principal Stress (ksi) (4)	Minimum Principal Stress (ksi) (4)	ρ (1)	Limit State Strain	Margin of Safety (2)
1 Foot Side Drop	NST	SA-212 GrB	0.002	38.0	-4.1	<0	0.159	79
	Skirt	A-36	0.015	38.1	-1.15	<0	0.129	7.6
	End Plate	A-36	0.114	54.6	-0.38	<0	0.129	0.13
30 Foot Side Drop	NST	SA-212 GrB	0.036	47.1	0.0	0	0.159	3.4
	Skirt	A-36	0.174	64.5	-25.5	<0	0.129	-0.26
	End Plate	A-36	0.676	148	-0.5	<0	0.129	-0.81
30 Foot Flat End	Skirt	A-36	0.005	38.2	0.0	0	0.129	25
	End Plate	A-36	0.034	49.5	-0.25	<0	0.129	2.8
30 Foot Round End	NST Domed End	SA-212 GrB	0.054	51.7	0.0	0	0.159	1.9
30 Foot Flat End Corner Drop (3)	End Plate	A-36	0.064	13.5	-51.5	<0	0.129	1.0
	Skirt	A-36	0.048	37.8	-17.0	<0	0.129	1.7
30 Foot Round End Corner Drop	NST Domed End	SA-212 GrB	0.150	77.4	-0.004	<0	0.159	0.06

(1) $\rho = \dfrac{\text{Minimum Principal Stress}}{\text{Maximum Principal Stress}}$

(2) Margin of Safety $= \dfrac{\text{Limit State Strain}}{\text{Maximum Principal Strain}} - 1$

(3) 20^0 Drop Angle

(4) At the location where maximum principal strain occurs

Table 4-3 Summary of impact analysis results for reactor pressure vessel.

Impact Orientation	Structure	*Maximum* Principal Stress (ksi)
1 Foot Side Drop	Nozzle/Vessel Junction	15.9 / 17.3
30 Foot Side Drop	Nozzle/Vessel Junction	90.0 / 82.1
30 Foot Flat End	Nozzle/Vessel Junction	40.1 / 40.1
30 Foot Round End	Nozzle/Vessel Junction	15.6 / 15.6
30 Foot Flat End Corner Drop	Vessel*	31.7
30 Foot Round End Corner Drop	Nozzle/Vessel Junction	89.8 / 70

* Nozzle is far away from the impact zone.

Table 4-4 Maximum value of stresses (ksi) and strains of a simplified model for various drop angle on the round end.

	Outer Shell				RPV
Drop Angle (Deg)	Effective Plastic Strain	Maximum Shear Strain	Maximum Effective Stress	Maximum Shear Stress	Effective Stress
15	0.0910	0.0580	53.4	29.8	25.0
30	0.0980	0.0789	54.6	31.1	25.1
62	0.1170	0.0833	56.5	32.7	26.8

Table 4-5 Maximum value of stresses (ksi) and strains of a simplified model for various drop angle on the flat end.

	Outer Shell				RPV
Drop Angle	Effective Plastic Strain	Maximum Shear Strain	Maximum Effective Stress	Maximum Shear Stress	Effective Stress
5	0.0580	0.0418	50.0	28.6	2.9
30	0.0194	0.0338	46.3	26.7	3.0
60	0.000	0.0048	41.3	23.0	5.3

Table 4-5 Maximum value of stresses (ksi) and strains of a simplified model for various drop angle on the flat end.

Drop Angle (degrees)	Max. Effective Plastic Strain in the Outer Shell	Max. Rigid Body Deceleration in the Lateral Direction ($in./sec^2$)
5	0.058	9380
10	0.059	5920
15	0.044	5290
20	0.032	3610
30	0.019	3220
62	0.000	2780

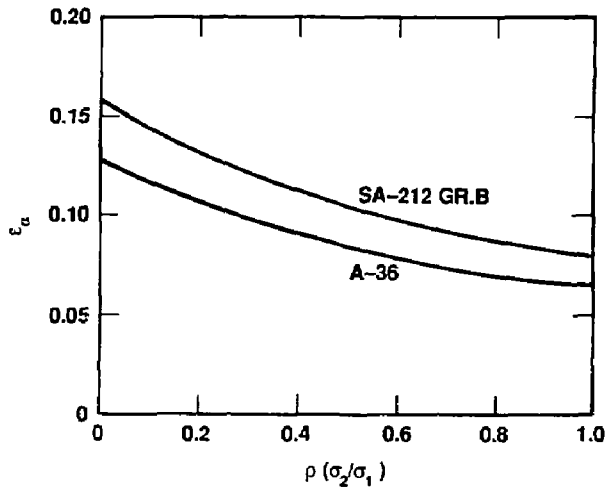

Figure 4-1 Strain limits for steels loaded biaxially.

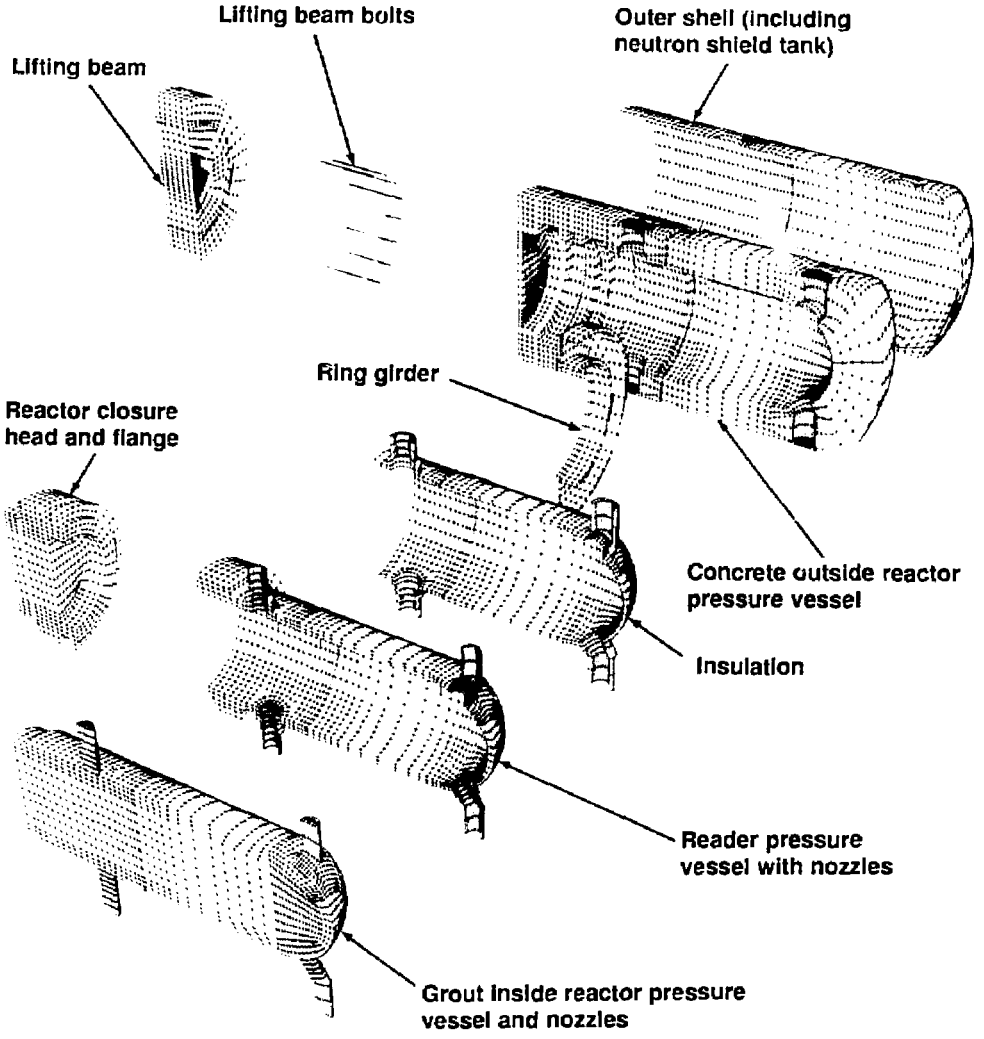

Figure 4-2 Full size complete model for Shippingport package.

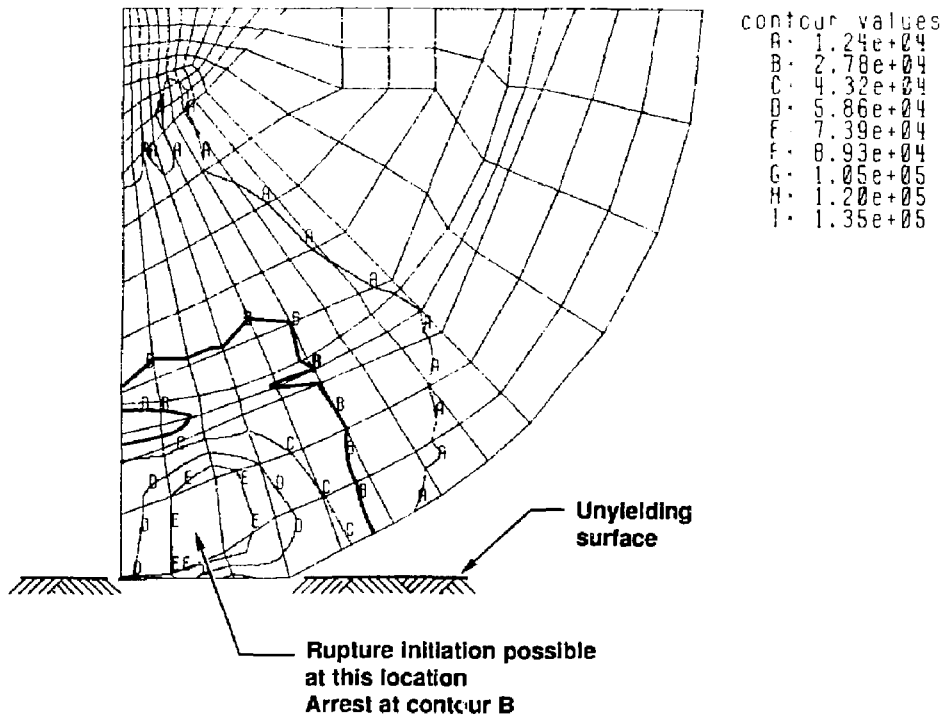

Figure 4-3 Contours of maximum principal stress in the lower end plate for 30 foot side drop.

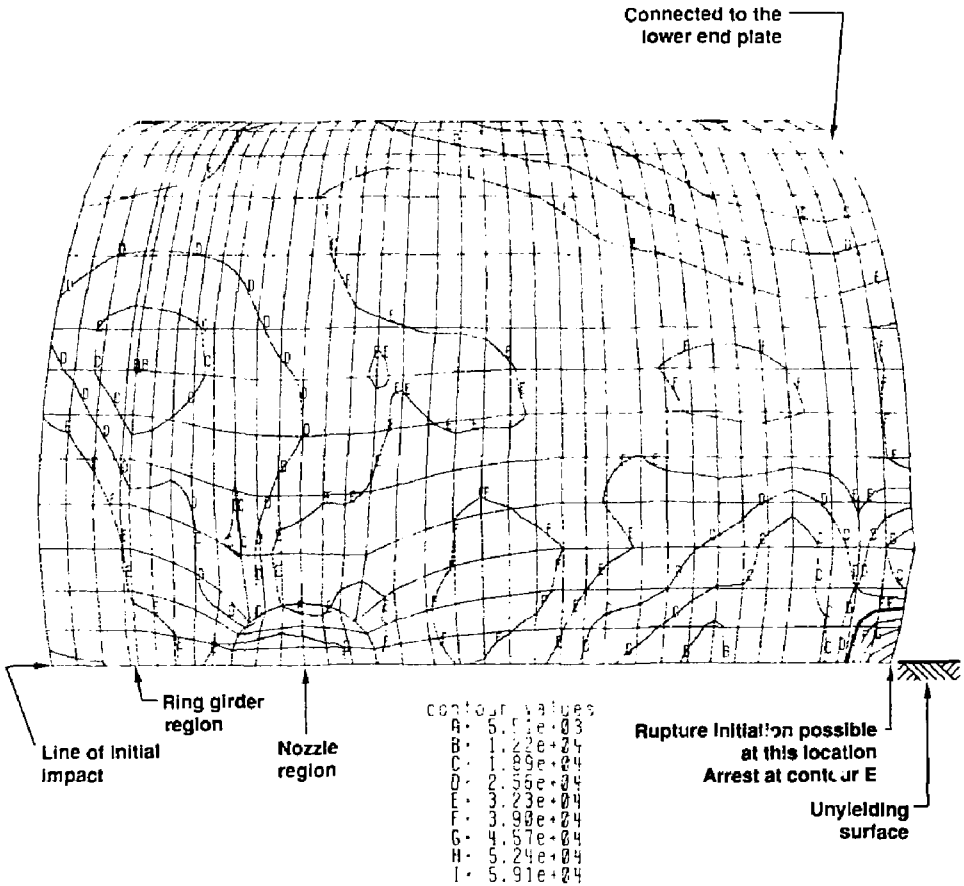

Figure 4-4 Contours of maximum principal stress in the skirt.

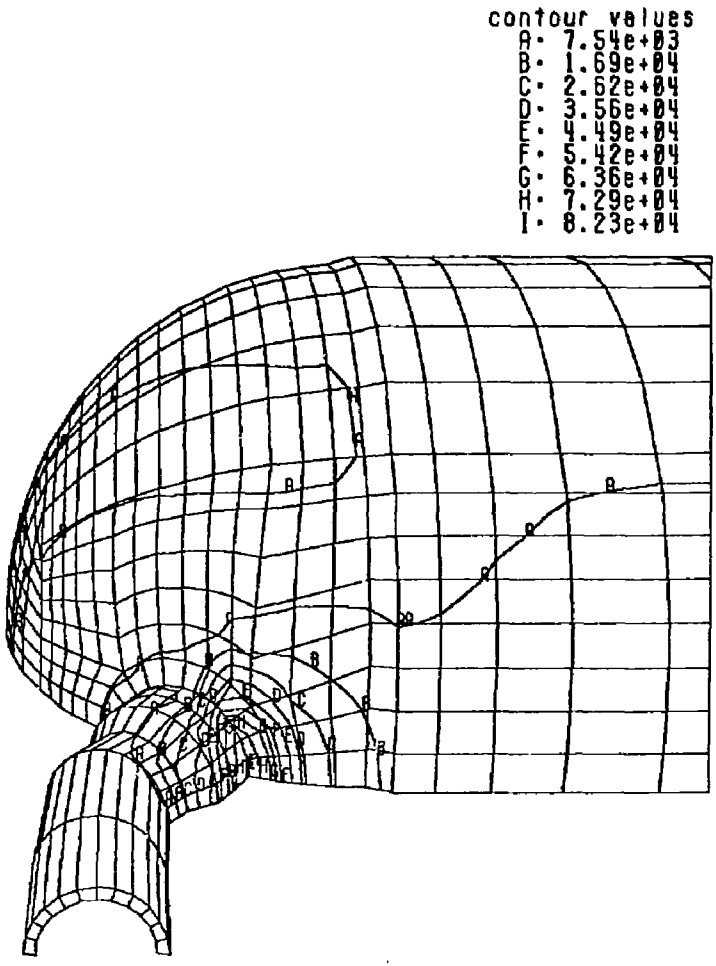

Figure 4-5 Contours of maximum principal stress in the nozzle/vessel junction for 30-ft side drop.

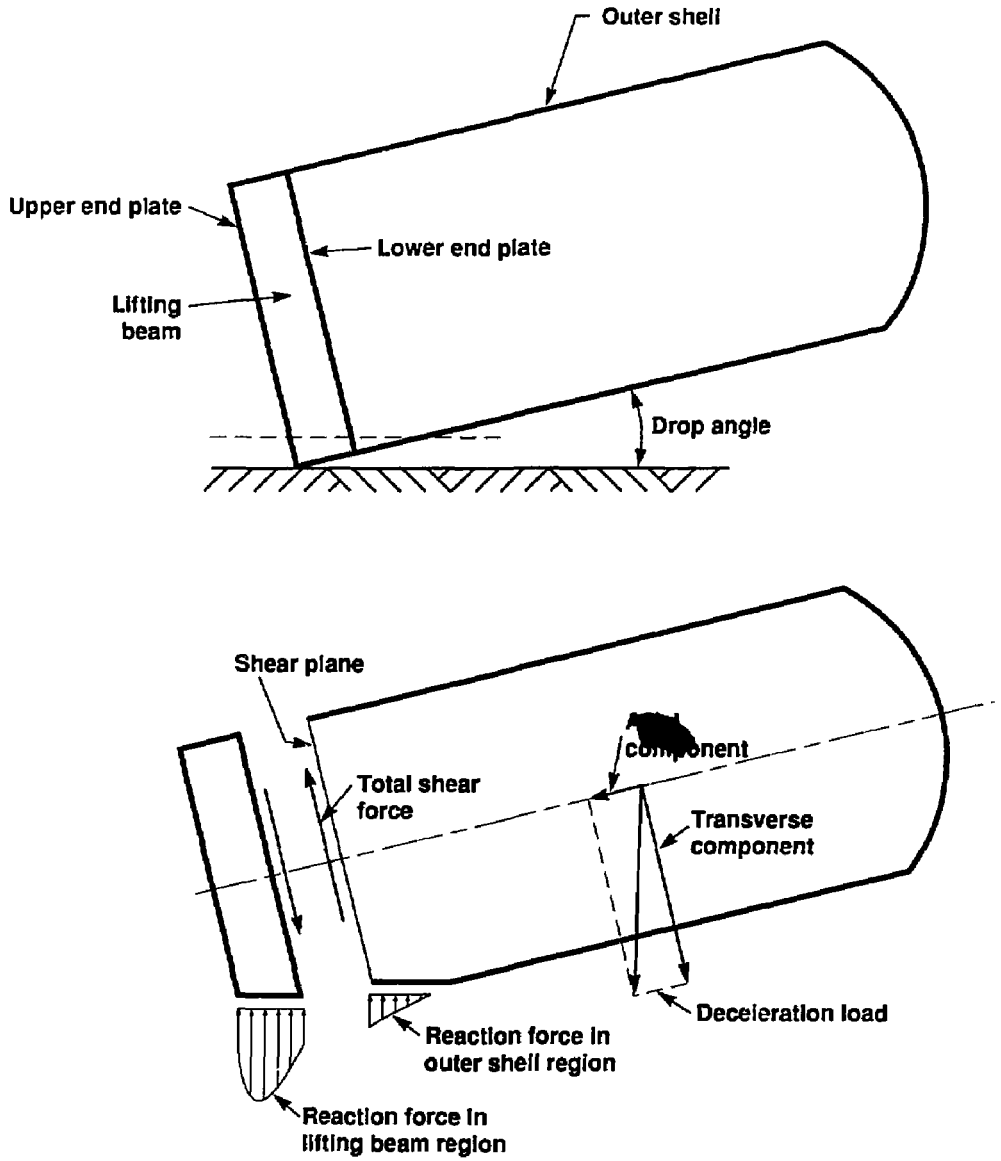

Figure 4-6 The lateral shear force and the reaction forces during deceleration of the package.

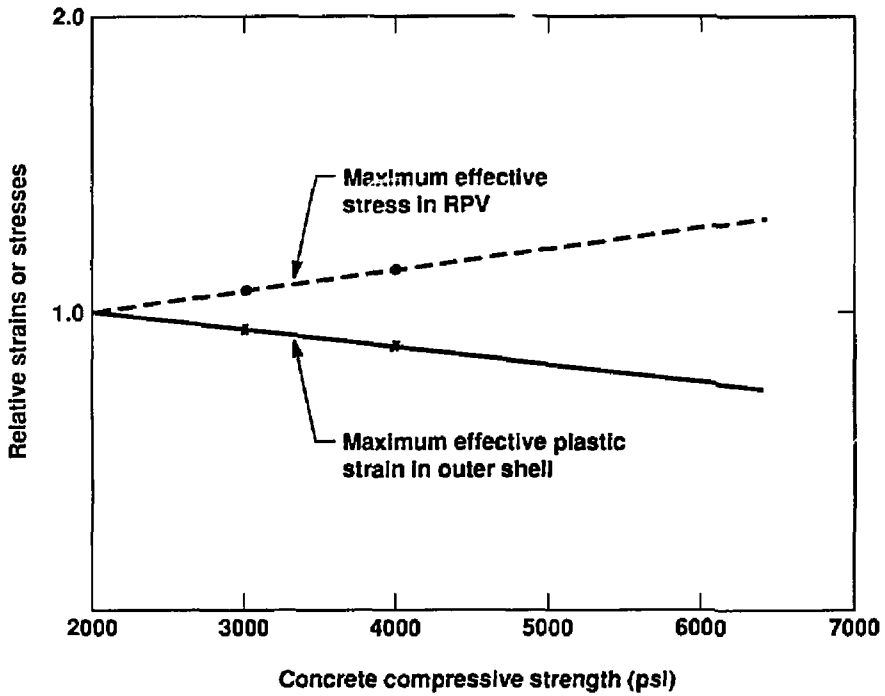

Figure 4-7 Effects of concrete compressive strength on the stresses and strains in the Shippingport package.

5.0 Structural Evaluation for Puncture Load

5.1 Introduction

The main concern in the puncture evaluation for the RPV/NST package (Figure 2-1) is to insure that any damage to the package due to puncture will not lead to the violation of external radiation standards and the dispersal limits set forth in 10 CFR 71.47 and 71.51 respectively. The NST and the concrete between the RPV and the NST are considered to be sacrificial material in puncture because the NST can still maintain its confinement function if punctured through by a 6-in.-diamater bar. A finite-element analysis using the LLNL computer code DYNA2D was performed to evaluate the RPV in accordance with the puncture requirements of 10 CFR 71.

5.2 Assumptions and Methods of Analysis

To simplify the analysis, no credit was taken for puncturing the outer shell and NST concrete. The 6-inch-diameter puncture bar was analyzed as punching through the NST and the concrete between the RPV and the NST without dissipating energy, and keeping its original configuration intact. The tangent surface of the RPV shell at the point of contact was modeled to be perpendicular to the axis of the puncture bar. This modelling approach avoids applying any bending moment to the bar which could cause the bar to collapse prematurely.

Because the curvature at any location of the RPV is much larger than the radius of the puncture bar, the effect of shell curvature is expected to be negligible. In this case, the most vulnerable location is where the RPV shell thickness is a minimum. Because the reactor closure head is extremely thick, there is little likelihood that it can be punched through by a 6-inch-diameter mild steel bar.

Figure 5-1 shows a 2-D finite-element analysis model at the start of RPV impact against the puncture bar. An enlarged plot of the lower portion of the RPV, including the puncture bar, is shown in Figure 5-2. The axis of the RPV is vertical and is aligned with the puncture bar in a CG (center of gravity)-

over-impact orientation. This orientation avoids any RPV rotation and provides maximum puncture energy. The shell thickness at the point of contact is 6.0 inches, the smallest in the RPV. It is the most vulnerable orientation for RPV-puncture bar impact. Thus, other puncture locations, including puncture on the side wall of the RPV, are not considered.

The interface friction between the puncture bar and the RPV was modeled in the analysis. The coefficient of friction used was 0.15, based on "Shock & Vibration Handbook" by Harris and Crede (Ref. 11).

The puncture bar is over 41 inches long and is long enough to reach the RPV. However, to reduce the amount of computer running time, the bar is assumed to be rigid except for the top 8 inches. This assumption is conservative because less energy is wasted in compressing the bar. The top 8 in. is sufficient to simulate the effects of plastic deformation of the puncture bar on the RPV.

The RPV is dropped from a height of 40 inches above the tip of the puncture bar. Thus, the RPV has a velocity of 175.8 in./sec at the start of the puncture analysis. With this drop height and package orientation, the lowest point of the RPV is at least 81 inches above the ground, an unusual height for such a large item like the Shippingport package.

In this puncture analysis, we used the mechanical properties of ASME SA212 Gr. B for the puncture bar (same material as the NST). This material has a yield strength of 38 ksi and can be considered a mild steel. All material were modeled in DYNA with unlimited strain-hardening capability.

5.3 Results of Finite-Element Analysis

The analysis was carried out for the first 24 ms of impact. Table 1 shows the axial deformation of the puncture bar and the average velocity of the RPV at 12 and 24 ms after impact. There is no need to analyze the problem beyond 24 ms because, by this time, the length of the puncture bar is reduced to less than half of its original length in the nonrigid region of 8 inches even though the RPV still has most of its kinetic energy left.

As the puncture bar undergoes axial plastic deformation at early stages of contact, the material flows in the radial direction, and the diameter of the bar is increased as shown in Figure 5-3 except along the RPV/puncture bar interface, where friction prevents relative motion between the RPV and the puncture bar. If no friction were modeled, the cross-sectional area at the point of contact would have expanded freely, as would the bar. At later times, the frictional force is overcome. The contact area is actually reduced, rather than increased, below the original cross-sectional area of the puncture bar. The side surface at the top of the puncture bar starts to touch the RPV at 19 ms. This, in effect, increases the interface area after it was initially reduced.

To determine if the puncture bar can punch through the RPV shell, we need an acceptable failure prediction method, such as Section III of the ASME Code. However, we have deep reservations about using the ASME code for puncture evaluation because the ASME Code focuses on normal loads (membrane or membrane plus bending) in dealing with problems associated with pressure vessels; however, for punctures of plates and shells, shear load is of major importance.

Much research work has been done by the shipping-cask industry in the past twenty years. Larder and Arthur (Ref. 12) proposed a failure prediction method for shipping casks. This method, as applied to the Shippingport package, is as follows:

> The RPV shell is punctured when the shear stress on a cylindrical surface concentric to the axis of the puncture bar (as shown in Figure 5-4) exceeds 60% of the material tensile strength throughout the thickness of the RPV except near the shell surfaces.

This method proposed by Larder and Arthur is further confirmed in an ongoing sensitivity study at LLNL under a different project using the DYNA2D and NIKE2D codes. Preliminary results of this sensitivity study indicate that this method predicts failure of a plate close to the mean of all existing test results on cask puncture, including the tests done by Larder and Arthur.

The RPV has a engineering tensile strength of 93 ksi. Therefore, the minimum shear strength for puncture evaluation is 56 ksi. In fact, the true material strength should be used instead of the engineering strength. However, it is conservative to use the engineering strength.

The critical stress occurs 19 ms after initial contact. Contours of y-z shear stress at this instantaneous time are shown in Figure 5-4. Please note that the orientation of the y-z shear stress is parallel to the imaginary surface.

Shear stress is zero at a free surface; it is very small near the surface of the steel at an interface of concrete and steel. Unless very fine meshes are used close to the interfaces, it is difficult for a plot routine to capture the dramatic change in shear stress close to the surfaces. This difficulty explains why many contours shown in Figure 5-4 intersect the surfaces of the RPV at a rather high level of shear stress. However, the use of a very fine mesh is not warranted here because no significant improvement in analysis results would be realized.

The critical imaginary cylindrical surface is marked with a dashed line. The minimum shear stress on this surface except close to the surface of the RPV shell is slightly above 15 ksi and is nowhere near the allowable of 56 ksi. The stress in the RPV actually decreased right after 19 ms because of the increase in the interface contact area.

5.4 Buckling of the Puncture Bar

In the previous section, the puncture evaluation of the Shippingport package is based on stresses generated in the RPV by the puncture bar. Because the puncture-bar material was assumed to have unlimited strain-hardening capability, the analysis was carried out far beyond the ultimate tensile strength of the puncture-bar material. The average axial compressive stress in the puncture bar reaches the ultimate tensile stress (70 ksi) in about 5 ms. The average axial stress at 19 ms is about twice the ultimate tensile strength as shown in Figure 5-5.

In reality, it is impossible for the real nonrigid bar to maintain its axisymmetric unbuckled position with that much plastic deformation. The puncture bar would have buckled long before reaching that state of deformation because of possible initial imperfections, such as the alignment of the contact surfaces and its material properties. It is also doubtful if the bar can maintain axisymmetric position even for 5 to 12 ms, which is the time the axial deformation of the bar reaches 15% to 25% of its initial non-rigid length.

According to the tangent-modulus theory of inelastic buckling (Ref. 13), a column buckles close to a load predicted by Euler's elastic-buckling formula, with Young's modulus replaced by the tangent modulus. Another approach, the reduced-modulus approach, predicts only a slightly higher buckling load than the tangent-modulus approach.

The tangent modulus of the mild steel and, therefore, the buckling load of the puncture bar becomes very small when the material is stressed far beyond the yield point. The possibility of reaching the stress state obtained by the finite-element analysis at 19 ms without buckling is practically nil.

5.5 Summary and Conclusion:

The assessments based on stresses described in Section 5.3 indicate that the RPV will not be punched through by the 6-inch-diameter puncture bar. The assessments were made for the critical stress state, which occurs 19 ms after initial contact, when the length of the puncture bar has already been significantly reduced.

The assessment based on the worst stress state at 19 ms is extremely conservative from the standpoint of inelastic buckling of the puncture bar. The bar will buckle long before the ultimate strength of the puncture-bar material can be reached, not to mention the stress state at 19 ms, which is twice the ultimate strength of the material.

It is clear that RPV will not be punched through by the puncture bar. However, if it did happen, a worst and unlikely scenario, the bar would be locked in place due to friction by the concrete and the NST steel shell. As a result, there would be no dispersal of radioactive material. Also, the

puncture bar itself will provide sufficient shielding in place of the material it displaces.

Table 5-1 Axial deformation of puncture bar and the average velocity of RPV.

Time (ms)	0	12	24
Puncture bar - Axial deformation (in.) (original length = 8 in.)	0.0	2.1	4.1
Average velocity of RPV (in./sec)	176	172	157

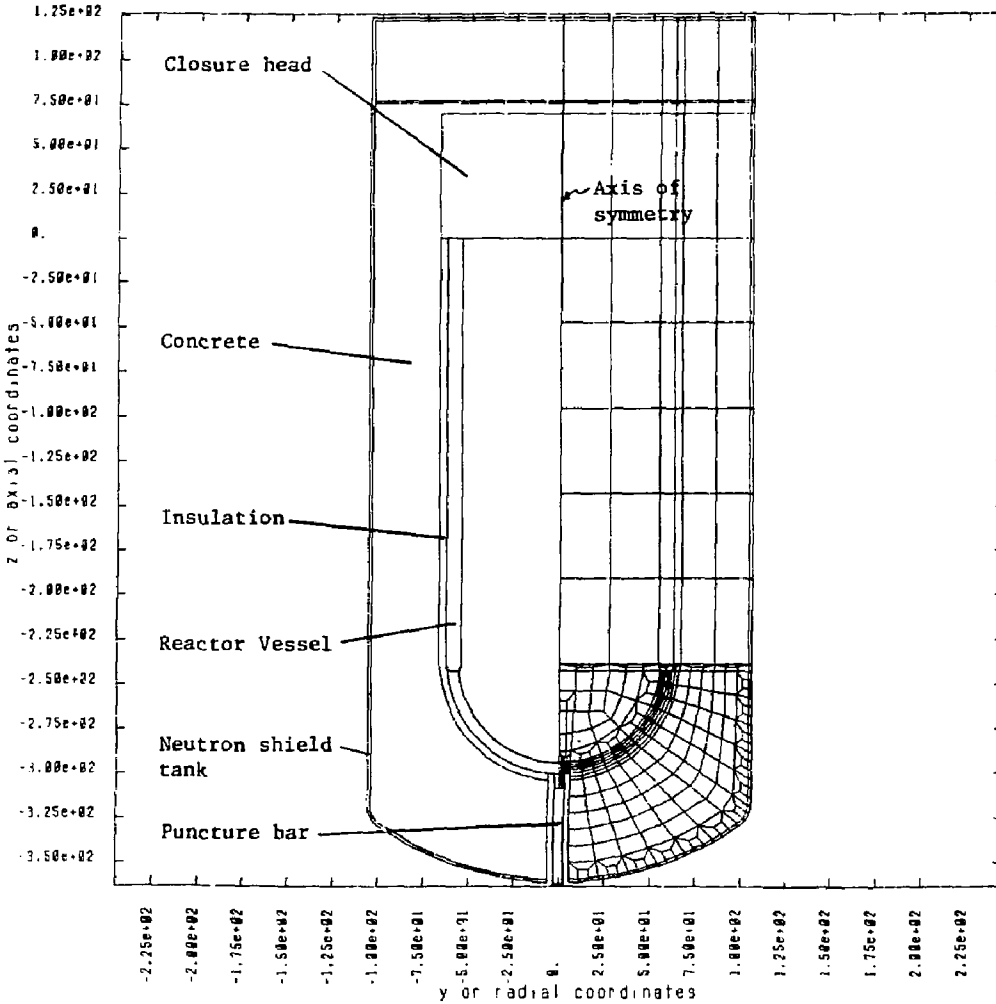

Figure 5-1 Axisymmetric finite element model of Shippingport package for puncture analysis.

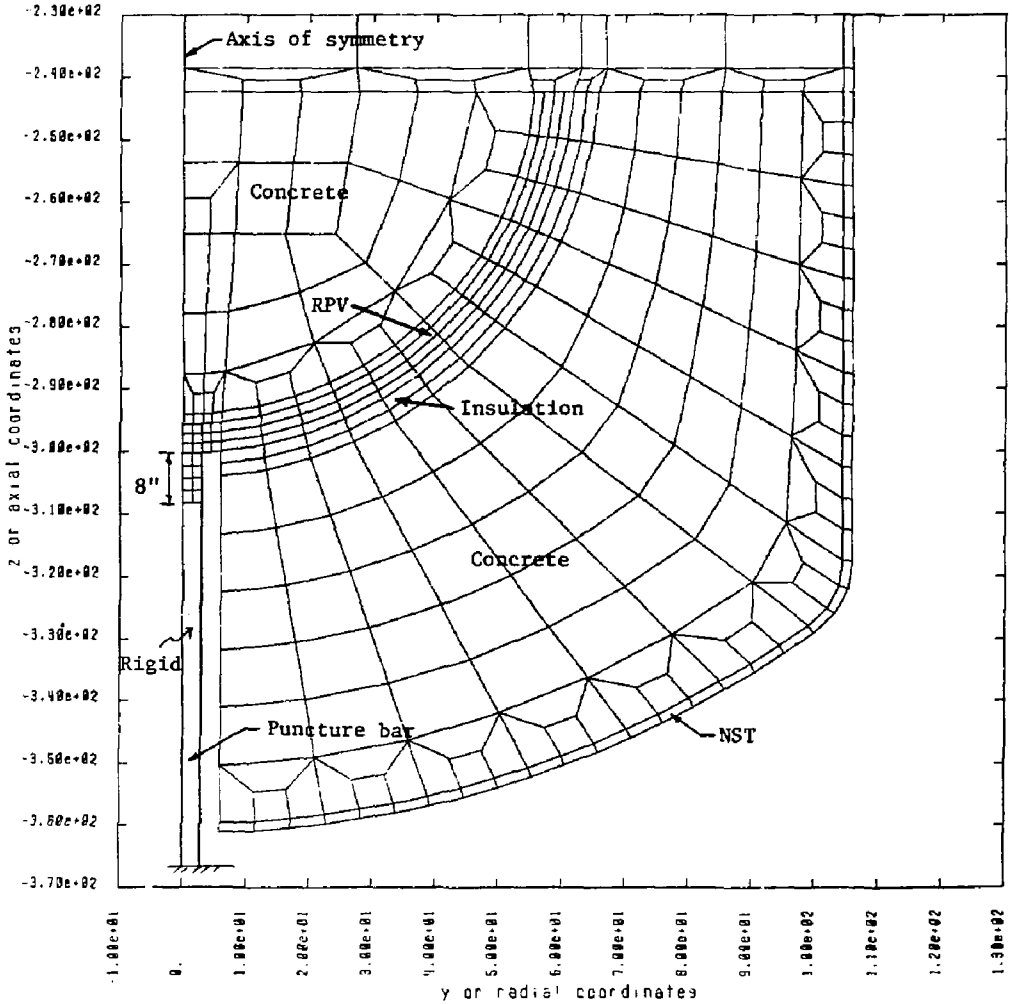

Figure 5-2 Lower portion of an axisymmetric finite element model under puncture load.

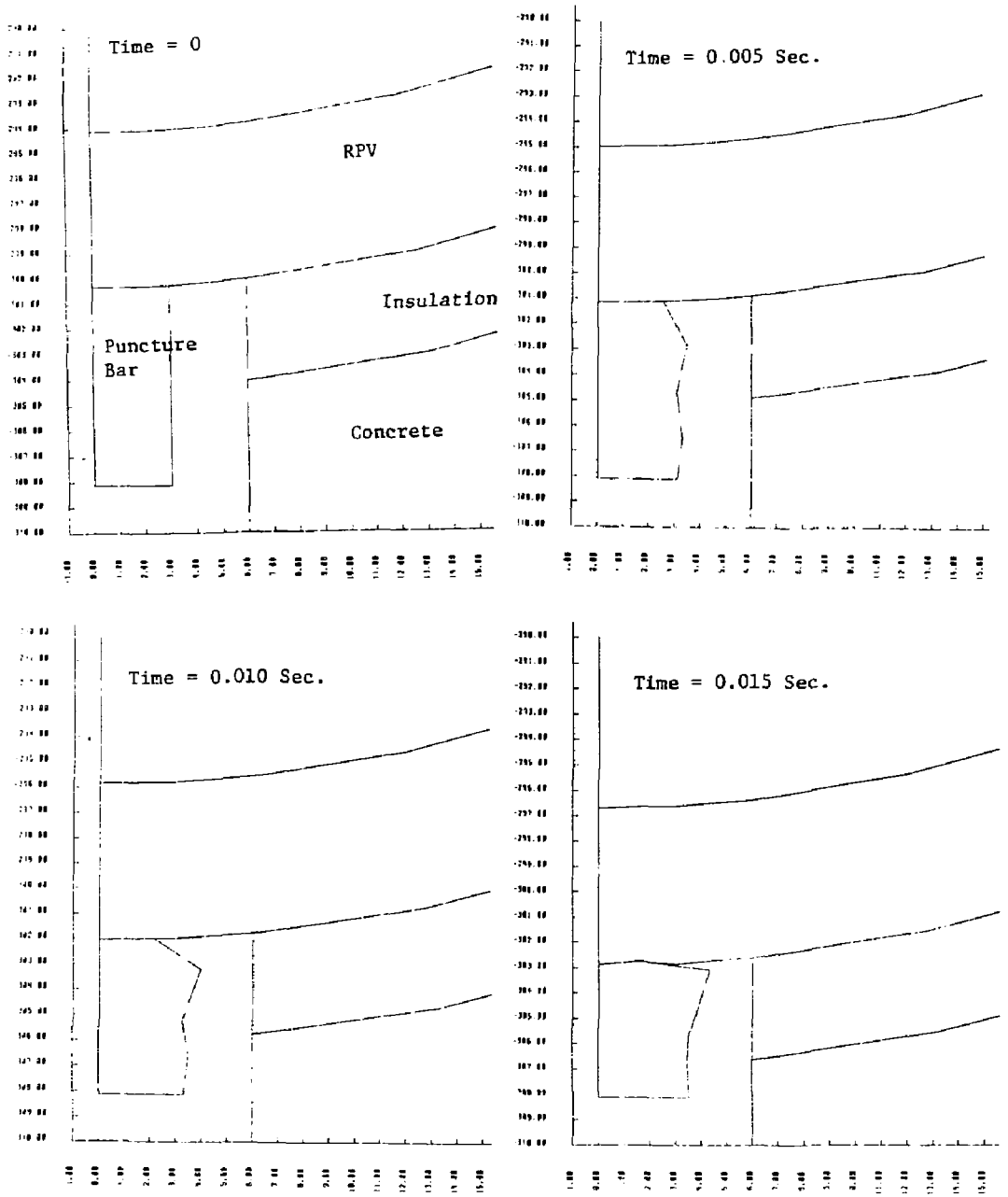

Figure 5-3 Axial deformation of reactor pressure vessel and puncture bar. (Units are in inches and seconds)

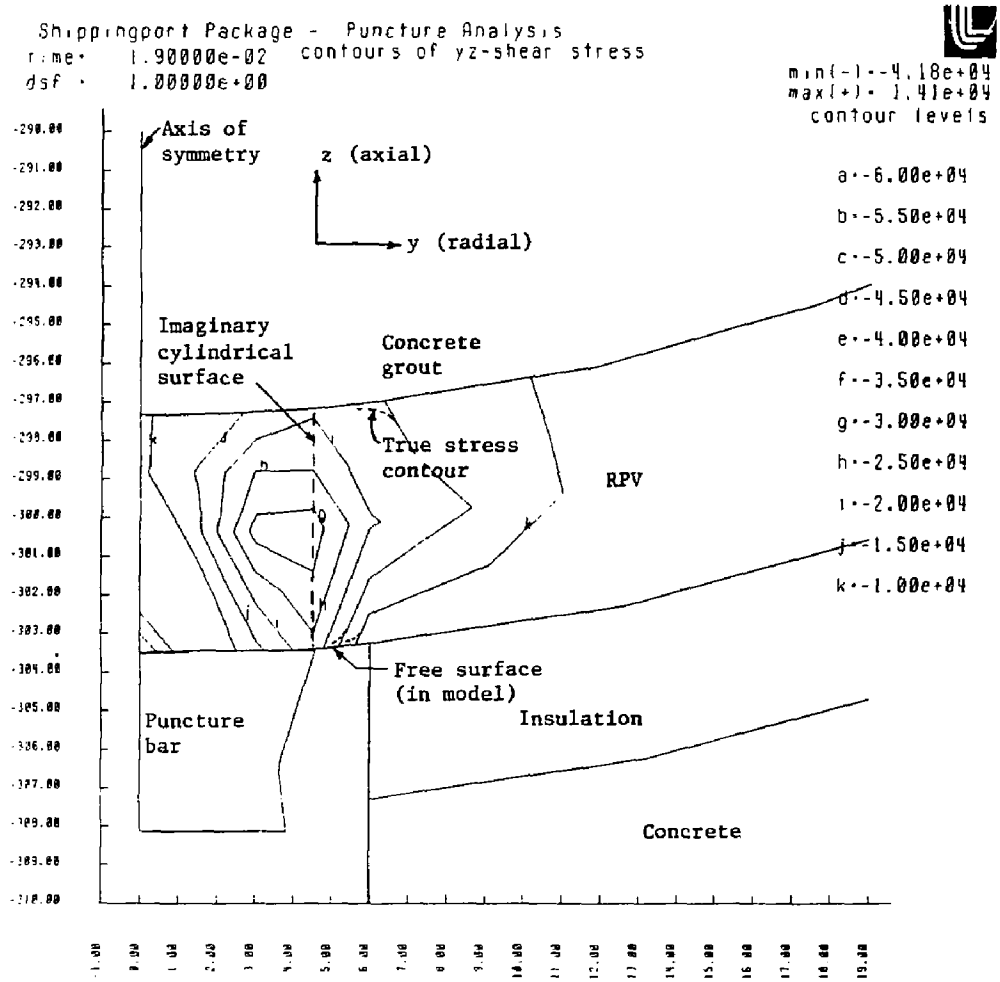

Figure 5-4 Contours of y-z shear stress at time = 0.019 sec. (Units are in inches, pounds, and seconds)

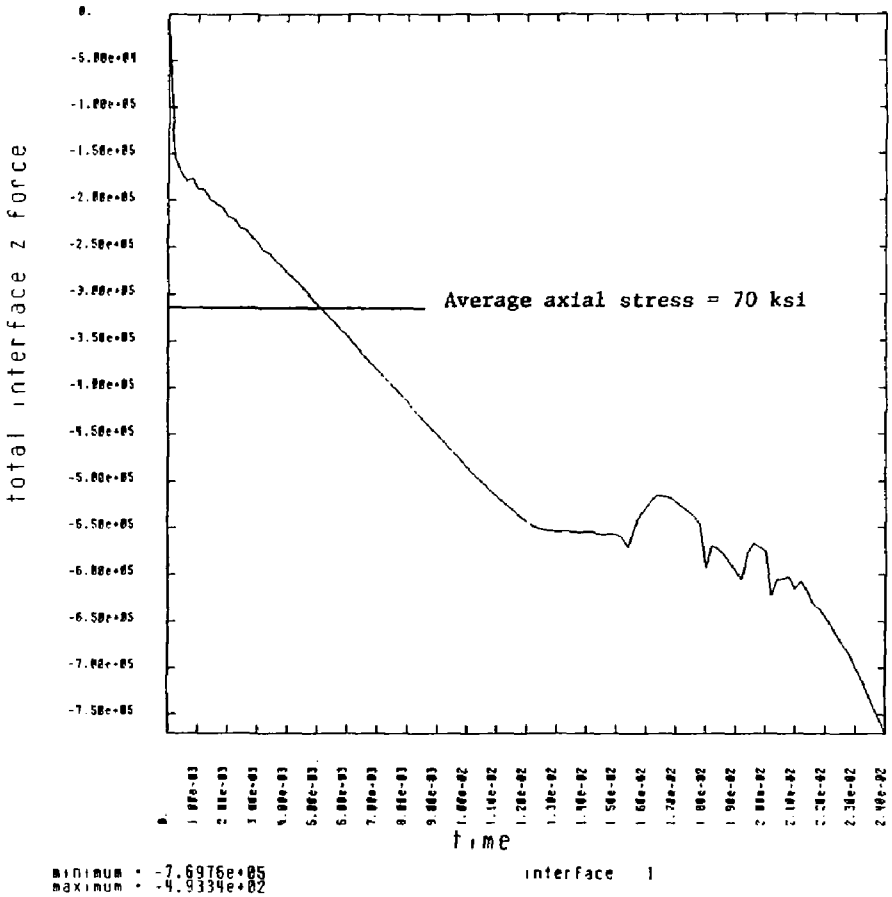

Figure 5-5 Interface force between RPV and puncture bar. (Units are in inches, pounds, and seconds)

References

1. J. O. Hallquist and D. J. Benson, "DYNA3D User's Manual, Nonlinear Dynamic Analysis of Structures in Three Dimensions," Lawrence Livermore National Laboratory, UCID-19592, Rev. 3, July, 1987.

2. J. O. Hallquist, "User's Manual for DYNA2D - An Explicit Two-Dimensional Hydrodynamic Finite Element Code with Interactive Rezoning," Lawrence Livermore National Laboratory, UCID-18756, Rev. 1, February, 1982.

3. "Packaging Review Guide for Reviewing Safety Analysis Reports for Packagings," UCID-21218, Lawrence Livermore National Laboratory, prepared for the U.S. Department of Energy, September, 1987.

4. "Preliminary Safety Analysis Report for Packaging - Shippingport Reactor Pressure Vessel and Neutron shield Tank Assembly," Westinghouse Hanford Company, prepared for the Shippingport Station Decommissioning Project, Department of Energy, 1988.

5. Shippingport Station Decommissioning Project, "Procedure for Batching, Mixing and Field Testing, Fill Material for Neutron Shield Tank and Lifting Beam and Skirt (Lightweight Grout), Rev. 3, General Electric Nuclear Business Operations, Shippingport, PA (January, 1988).

6. J. W. Simons and P. R. Gefken, "Characterization of Grout for DYNA3D Model," SRI International, prepared for the Lawrence Livermore National Laboratory, April, 1988.

7. M. A. Gerhard, "SLIC: An Interactive, Graphic Mesh Generator for Finite Element and Finite-Difference Application Programs," Lawrence Livermore National Laboratory, UCRL-52823, September 13, 1979.

8. C. E. Wilson and L. H. Goldmann, "Test Procedures for Drop Testing of the Shippingport RPV/NST Benchmark 1/10 Size Models," SPC-TP2-0001, Rev. 0, Westinghouse Hanford Corp, (February 11, 1988).

9. L. H. Goldmann, Shippingport Benchmark Test for the 1/5 and 1/10 Size Models - data Compilation Report, SSDP 0049, June 1988.

10 Mendelson, A., "Plasticity: Theory and Application," the Macmillan Co., New York, 1968, p. 8.

11 9.C. M. Harris and C. E. Crede, Shock and Vibration Handbook, second edition, McGraw-Hill, 1976.

12. R. A. Larder and D. Arthur, "Puncture of Shielded Radioactive Material Shipping Containers," Lawrence Livermore National Laboratory, UCRL-52836; Prepared for the U.S. Nuclear Regulatory Commission, NUREG/CR-0930, December, 1978.

13. "Guide to [illegible] Structure," edited by Bruce G. Johnston [illegible] Council, Third Edition, John Wiley & Sons, 197[illegible].